



ORIGINAL PAPER

Harshal P. Mahamure · Vagesh D. Narasimhamurthy ·
Lihao Zhao

Planar shear flow effects on particle dispersion over a normal flat plate

Received: 8 January 2022 / Revised: 9 July 2022 / Accepted: 2 August 2022 / Published online: 24 September 2022
© The Author(s), under exclusive licence to Springer-Verlag GmbH Austria, part of Springer Nature 2022

Abstract We investigate the effect of planar shear inflow on the dispersion of inertial particles in the unsteady laminar wake behind a normal flat plate and the corresponding particle deposition on the plate. Eulerian–Lagrangian simulations are performed to solve the dilute particulate suspension flow over the plate. To explore the effect of shear, we perform a comparative assessment between two different cases, distinguished based on their inflow profiles, namely uniform and linear shear flow (with shear parameter $K = 0.1$). Flow Reynolds number based on the mean inflow velocity is 60 in each case, where the unsteady wake is characterized by von Kármán vortex street. Three different classes of particles are tracked in each case, where each particle class is characterized by its Stokes number (St), namely $St = 0.1$ (low), $St = 1$ (medium), $St = 10$ (high). Flow visualizations show that planar shear alters the vortex shedding pattern, especially at far downstream positions. Such changes in the wake flow lead to significant streamwise stretching and rotation of particle-depleted void regions and adjacent particle clusters. With the help of Voronoï diagrams, we characterize fluid shear driven changes in inhomogeneous particle distribution patterns and lateral shifts in positions of particle clusters observed for each St-class of particles. The quantitative effect of shear on the dispersed phase statistics of each St-class of particles is further analyzed. Such effects are not appreciable near the plate, but become evident further downstream away from the plate. At such positions, the impact of shear on the concentration of medium St-class particles is the most significant among all classes, where the mean particle concentration near the wake centerline is significantly increased. Furthermore, local peaks in particle concentration profiles and minima in particle velocity profiles shift laterally in their positions toward the low-stream region due to the shear. The shear also causes a marginal reduction in particle deposition efficiency.

1 Introduction

Understanding the transport of tiny inertial particles suspended in laminar or turbulent carrier flow is crucial in many diverse fields of human life. The knowledge and quantitative prediction of such two-phase flows have significant importance in fields like respiratory health (e.g., transport of inhaled airborne particles through animal respiratory tracts), natural flows (e.g., eolian sediment transport), environmental pollutant dispersion, and industrial appliances (e.g., atomizers)—to name a few. Besides the relevance of particle-laden flows in

Supplementary Information The online version contains supplementary material available at <https://doi.org/10.1007/s00707-022-03327-y>.

H. P. Mahamure (✉) · V. D. Narasimhamurthy
Department of Applied Mechanics, Indian Institute of Technology Madras, Chennai 600 036, India
E-mail: am17d012@smail.iitm.ac.in

L. Zhao
AML, Department of Engineering Mechanics, Tsinghua University, 100084 Beijing, China

various fields, the physics of such flows exhibits interesting features such as preferential concentration in strain-dominated regions of the flow field [1], and turbophoretic particle migration in wall-bounded turbulent flows [2]. Of particular interest to our study is the particle-laden flow past an obstruction (i.e., bluff body), which has significance in a wide range of engineering applications. Some examples of applications are baghouse dust collectors used for separating dust particles [3], particle deposition on heat exchanging components in coal-fired plants [4], volcanic ash deposition over blades of gas turbine aero-engines, etc. The significance of such flows explains why several studies performed so far (in a bounded or unbounded domain) focused on predicting inertial particle deposition over an obstruction and their dispersion in the wake region of flow (see [5–14]). Aforementioned studies considered a generic two-dimensional bluff-body obstruction to minimize uncertainty due to geometric complexity. Before we proceed, it is useful to introduce a couple of dimensionless parameters associated with particulate suspension flows over an obstruction that dictates their physical behavior, viz., the flow Reynolds number (Re) and particle Stokes number (St). The flow Reynolds number (Re) is often defined on the basis of the characteristic dimension of the bluff body (l_c), characteristic (i.e., inflow) velocity (U_c), and fluid kinematic viscosity (ν_f) as $Re = U_c l_c / \nu_f$. Flow features such as vortex shedding, forces exerted by the fluid on the body, and dispersion of particles in the wake region are strongly dependent on Re . The particle Stokes number (St), defined as the ratio of particle relaxation time (τ_p) to the characteristic flow time scale (τ_f), plays a prominent role in dictating the fluid–particle hydrodynamic interaction.

Some studies have focused on studying the motion of particles of different Stokes numbers in unsteady flows behind a rectangular cylinder placed in a channel and their subsequent deposition over the cylinder. Brandon and Aggarwal [5] performed simulations to study the deposition of $St = 0.01$ – 5 particles over a square cylinder in a channel at Re values ranging from 200 to 2000. They reported that Re had an insignificant effect on particle deposition but a noticeable effect on particle dispersion and distribution. They also highlighted that particle deposition increased rapidly with St from 0 to 1 but became less sensitive to St above unity. The effect of blockage and aspect ratio¹ of a rectangular obstruction on particle transport and deposition was studied by Salmanzadeh et al. [6]. They found that particle deposition increased with blockage ratio; however, it was not influenced significantly by changes in the aspect ratio. Afrouzi et al. [7] quantified the effect of the streamwise flow pulsation amplitude on vortex shedding and particle deposition efficiency on a square cylinder. The other studies performed in similar flow configurations include Jafari et al. [8] and Bagheri and Sabzpooshani [9].

A considerable body of literature is also devoted to study particulate suspension flows over a circular cylinder either in a confined or unconfined situation. While investigating the particle dispersion in the wake of a circular cylinder, Yao et al. [10] found that Re and St have considerable effects on particle dispersion. Besides highlighting that particle dispersion increased with Re , they also elucidated the formation of organized distinctive particle dispersion patterns in the vortex street for each St value. They found that interaction of particles with the vortex street was exclusive to their inertia. They also reported that small St particles ($St = 0.01$) could enter vortex core regions, intermediate St particles ($St = O(1)$) concentrated at vortex boundaries, and large St particles ($St = 10$) mostly preferred to stay away from the vortex street. Haugen and Kragset [11] investigated distinct impaction modes of inertial particles (in $St = 0.01$ – 40 regime) on front- and back-sides of a circular cylinder at Re values ranging from 20 to 6600. Zhou et al. [12] studied the effect of inertia of particles (in $St = 0.01$ – 10 regime) on their distribution in the wake of a circular cylinder at different Re . They observed that particle distribution was strongly dependent on both Re and St . While analyzing the particle dispersion in the flow over a circular cylinder at $Re = 100$, Shi et al. [13] observed clustering of particles in the form of a bow-shock, and the shape of a cluster was found to be dependent on particle Stokes number (St). Recently, Shi et al. [14] analyzed the organized particle motion in von Kármán vortex street from a circular cylinder to find that the centrifuging of inertial particles from von Kármán vortex cores leads to the formation of coherent void hole regions. Particulate flows over triangular [15] and elliptical cylinders [16] have also been studied to a limited extent.

As noticed above, previous studies were performed on the particle-laden flow over a two-dimensional ($2D$) obstruction of generic shape (square, rectangular, circular, and triangular cylinders). However, surprisingly, the problem of particle-laden flow over a normal flat plate has received minimal attention, except for Chein and Chung [17] and Gomes and Vincent [18]. A normal flat plate is a limiting case of a rectangular cylinder of low aspect ratio. Nevertheless, flow over a plate is expected to evolve differently compared to a rectangular (or square) cylinder due to the absence of an afterbody and trailing edge separation phenomenon in the former. Similarly, flow around the plate should be different from a circular cylinder since flow separation points are fixed at leading edges of the former, while such flow separation points vary their positions on the surface with Re for the latter. The unique geometric shape and distinct flow patterns around the plate could bring appreciable

¹ The aspect ratio for a rectangular obstruction is defined as its width-to-height ratio.

changes in trajectories of particles in the vicinity of the body and their dispersion in the wake compared with square or circular cylinders.

Earlier studies on flow (without particles) past a bluff body have demonstrated remarkable effects of shear in the inflow on wake behavior. For instance, while studying the effect of linear shear inflow on vortex shedding and wake formation from a square cylinder for different shear rates, Cheng et al. [19] discovered that shear suppresses the vortex shedding. Furthermore, both lift and drag forces acting on the cylinder decreased with an increase in shear rate. Lankadasu and Vengadesan [20] suggested that critical Re at which flow changes its state (from steady to unsteady) decreased with the shear rate of linear shear inflow. In light of findings reported in the above studies, it is intriguing to know the effect of shear in the approaching carrier flow on the deposition and dispersion of suspended inertial particles, while no such information is available in the literature. The proposed study is aimed toward this end. We shall consider only planar shear as the background shear for the sake of simplicity and brevity in the present study.

We investigate the problem of particle-laden flow past a normal flat plate in the present work using computer simulations. For simplicity and brevity, the focus of our study is restricted to the laminar flow of dilute suspension over the plate. A primary goal is to understand and quantify the effect of planar shear inflow on the dispersion of particles in the laminar wake and their deposition over the plate. For such a purpose, we run two distinct sets of simulations, one with uniform inflow and another with linear shear inflow, and present our findings in the form of both qualitative and quantitative comparisons.

The content in this paper is organized in the following order. The numerical methodology implemented in the code and its validation are presented in Sect. 2. We then briefly introduce the problem considered for the present study in Sect. 3, followed by the discussion of results in Sect. 4. Concluding remarks are presented in the final Sect. 5.

2 Numerical methodology

We use Eulerian–Lagrangian hybrid frameworks to study laminar particulate suspension flow around a normal flat plate. The carrier phase is simulated in the Eulerian framework. It is considered to be isothermal and Newtonian, and is governed by the incompressible Navier–Stokes equations², which are given as

$$\nabla \cdot \mathbf{u}_f = 0, \quad (1)$$

$$\rho_f \left\{ \frac{\partial \mathbf{u}_f}{\partial t} + \mathbf{u}_f \cdot \nabla \mathbf{u}_f \right\} = -\nabla p + \mu_f \nabla^2 \mathbf{u}_f + F_{ib}, \quad (2)$$

where symbols \mathbf{u}_f and p represent the instantaneous flow velocity and pressure, respectively, while ρ_f and μ_f represent the fluid density and viscosity, respectively. The term F_{ib} in Eq. (2) is the direct forcing term used in the immersed boundary method (IBM) employed for handling the effect of bluff body on the carrier flow [21]. The scalar quantity is denoted using a regular symbol, while the vector quantity is denoted using a boldface symbol in this paper. If the subscripts f and p are present in a symbol, they denote the fluid and particle phases, respectively. Equations (1) and (2) are solved numerically on a staggered Cartesian grid with a finite-volume solver MGLT [22]. Convective and diffusive fluxes are discretized using the second-order accurate central differencing scheme. Explicit third-order accurate Runge–Kutta scheme is used to advance these discretized equations in time. This scheme is conditionally stable in nature. Therefore, time step size Δt_f should be below the limit specified by the Courant–Friedrichs–Lewy (CFL) criterion. The Poisson equation for the pressure is solved to ensure mass conservation by employing Stone’s [23] strongly implicit procedure (SIP).

The dispersed (particle) phase is simulated in the Lagrangian framework using a newly developed particle solver LaParT. It comprises of N_p number of non-reacting, solid spherical particles. Each particle considered here is significantly denser than the fluid, with a particle-to-fluid density ratio $(\rho_p/\rho_f) \approx O(1000)$. Furthermore, the diameter (d_p) of each particle is smaller than the characteristic hydrodynamic length scale (l_c) of the carrier flow, and therefore, it is treated as a point-particle. If $\mathbf{u}_f = \mathbf{u}_f(\mathbf{x}_p, t)$ is the instantaneous undisturbed fluid velocity at particle position $\mathbf{x}_p(t) = \mathbf{x}_p$ at time t , $\mathbf{u}_p = \mathbf{u}_p(t)$ is the instantaneous particle velocity at time t , then the Reynolds number associated with any particle based on the slip velocity ($\mathbf{u}_f - \mathbf{u}_p$) is given by $Re_p = \rho_f d_p |\mathbf{u}_f - \mathbf{u}_p| / \mu_f$. The motion of a particle through the non-uniform flow is governed by the

² Note that the two-phase mixture is treated as a dilute suspension. Thus, there is no feedback (from the dispersed phase to the carrier phase) force term appearing in Eq. (2).

Maxey–Riley equation [24], which is given as

$$m_p \left[\frac{d\mathbf{u}_p}{dt} \right] = \mathbf{F}_d + \mathbf{F}_b + \mathbf{F}_{pg} + \mathbf{F}_{am} + \mathbf{F}_{bh}. \quad (3)$$

Terms on the right-hand side of Eq. (3) are various forces acting on the particle. These forces (from left to right) are the Stokes drag (\mathbf{F}_d), buoyancy (\mathbf{F}_b), pressure-gradient (\mathbf{F}_{pg}), virtual-mass (\mathbf{F}_{am}), and Basset history (\mathbf{F}_{bh}). If the particle-to-fluid density ratio (ρ_p/ρ_f) $\approx O(1000)$, then effects of \mathbf{F}_{pg} , \mathbf{F}_{am} , and \mathbf{F}_{bh} on particle motion could be ignored [25]. Some studies also include the lift force term in Eq. (3), which is not present in the original equation. Mollicone et al. [26] simulated the particle-laden turbulent flow over a bump inside a channel. They studied the effect of the lift force³ on the mean concentration of particles of different Stokes numbers (based on the viscous scaling). They found that the mean concentration of particles, especially those having intermediate Stokes numbers, was significantly modified due to the lift force. Marchioli et al. [48] analyzed the role of gravity and lift forces⁴ on velocity statistics and deposition rates of particles in a vertical channel. They suggested that gravity and lift forces could quantitatively modify the dispersed phase statistics. They also mentioned that lift force significantly influenced the particle accumulation near the wall. On the contrary, Arcen et al. [28] reported that the inclusion of lift force⁵ in the equation of particle motion had an insignificant effect on the particle phase statistics in the absence of gravity. It appears from the literature that a widely accepted unique lift force model is still being explored. The effects of lift and near-wall forces on phenomena such as particle dispersion statistics and particle deposition are yet to be completely known and could be dependent on the choice of the model. Nevertheless, particles considered in the present study have small sizes, thereby, lift forces acting on such particles are negligible. Furthermore, the gravity force acting on a particle is not considered to isolate the Stokes drag force effect. The simplified Maxey–Riley equation describing a particle’s motion thus only contains the inertia and Stokes drag force. It can be written as

$$m_p \left[\frac{d\mathbf{u}_p}{dt} \right] = 3\pi\mu_f d_p \gamma (\mathbf{u}_f - \mathbf{u}_p). \quad (4)$$

The drag force term appearing on the right-hand side of the Eq. (4) is given using a nonlinear Stokes drag model. The empirical correction coefficient γ included in this term accounts for the large particle Reynolds number (Re_p) effects if the latter exceeds above unity. The coefficient γ is given as $\gamma = (1 + 0.15\text{Re}_p^{0.687})$ [29]. Equation (4) can be re-arranged as

$$\frac{d\mathbf{u}_p}{dt} = \frac{\gamma}{\tau_p} [\mathbf{u}_f - \mathbf{u}_p], \quad (5)$$

where parameter τ_p is the particle relaxation time given by $\tau_p = \rho_p d_p^2 / 18\mu_f$. The relaxation time of an inertial particle is the time taken by a particle to respond to the changes in the velocity field of the carrier flow. An exhaustive discussion concerning the above Eqs. (3–5) can be found in the review articles on Lagrangian methods for dispersed two-phase flows (see Minier and Peirano [30], Subramaniam [31], and Minier [32]). Additionally, we solve the equation of particle position, which is given by

$$\frac{d\mathbf{x}_p}{dt} = \mathbf{u}_p. \quad (6)$$

The Lagrangian solver LaParT, which is one-way coupled to the Eulerian solver MGLET, is used to solve the above Eqs. (5) and (6). In order to solve Eq. (5), we need to know the fluid velocity \mathbf{u}_f (i.e., $\mathbf{u}_f(\mathbf{x}_p(t), t)$) at the instantaneous particle position $\mathbf{x}_p(t)$. Three-dimensional reconstruction of the velocity field from the neighboring grid nodes to the instantaneous particle position is required to know \mathbf{u}_f . A second-order accurate trilinear scheme based on 2^3 points for the fluid velocity interpolation is used in this study. A second-order accurate Adams–Bashforth scheme is used to numerically integrate Eq. (5). The numerical methodology implemented in the LaParT to solve Eqs. (5) and (6) is discussed in “Appendix A” (also see Fig. 11)).

Before proceeding with the current problem, the Eulerian–Lagrangian solver (MGLET–LaParT) is validated first. The deposition efficiency of particles (η) of different Stokes numbers ($\text{St}=0.1, 1, 5$) over a square cylinder in a channel flow is compared against the reference data available in the literature in Fig. 1. Our simulation results are in agreement with the reference data. An extensive discussion on the verification and validation of MGLET–LaParT is included in “Appendix B”.

³ The lift force model used in this study is dependent on the fluid vorticity.

⁴ The lift force model used here considers the effect of finite particle Reynolds number, Re_p .

⁵ The lift force is accounted using the optimum lift force model, which includes the combined effect of shear and near-wall forces.

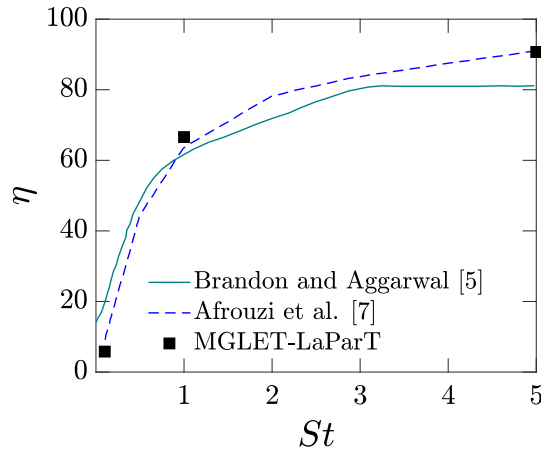


Fig. 1 Comparison of particle deposition from the simulation against reference data for different St values viz., $St=0.1, 1,$ and 5

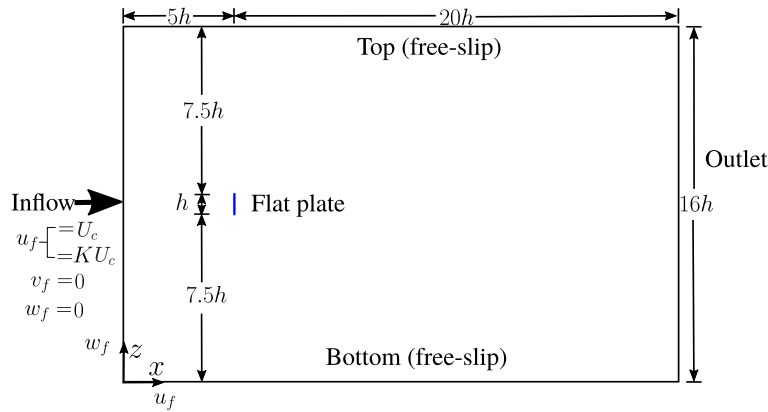


Fig. 2 Computational domain (not to scale)

3 Problem description

3.1 Carrier fluid

We consider the laminar flow of a viscous incompressible carrier fluid over a normal thin flat plate with a streamwise thickness of $0.02h$. The current plate configuration is similar to other wake studies [33–35]. Two-dimensional ($2D$) view of the computational domain (in an xz -plane) and the corresponding dimensions are shown in Fig. 2. Here, the x -, y -, and z -axes are aligned in the streamwise, spanwise, and cross-stream directions. From now on, all geometric dimensions are expressed in terms of the plate height h (i.e., reference length scale), and velocities are mentioned in terms of average⁶ inlet fluid velocity U_c (i.e., characteristic velocity scale). The computational domain size in the x , y , and z directions is $L_x = 25h$, $L_y = 0.25h$, and $L_z = 16h$, respectively (where L_x and L_z dimensions are similar to other wake studies [33–35]). Note that the numerical solver is three-dimensional, therefore, the domain is extended along the span (y) to a minimal extent ($0.25h$). We have chosen two cases for the present study, based on the fluid velocity profile at the domain inlet viz., uniform and linear shear inflow. It is worth highlighting that the average inlet fluid velocity U_c in both cases is the same. However, the local fluid velocity imposed at the inlet in the shear flow case increases linearly in the cross-stream (z -) direction with a fixed shear parameter $K = 0.1$, which is given as

$$K = \frac{h}{U_c} \left(\frac{\partial u_f}{\partial z} \right)_{x=0}. \tag{7}$$

⁶ The average implies that the steady inflow fluid velocity is averaged in the cross-stream (z) direction across the full domain height.

Table 1 The spatial and temporal discretization

Parameter	Value
$N_x \times N_y \times N_z$	$368 \times 5 \times 260$
$\Delta x_{\min}, \Delta x_{\max}$	0.0066h, 0.12h
Δy	0.05h
$\Delta z_{\min}, \Delta z_{\max}$	0.025h, 0.11h
Δt_f	$0.001h/U_c$

N_x , N_y , and N_z are the numbers of grid cells used for the simulation in the streamwise (x), spanwise (y), and cross-stream (z) directions, respectively. Δx_{\min} and Δx_{\max} are the minimum and maximum grid-cell sizes in the x -direction, while Δz_{\min} and Δz_{\max} are the corresponding sizes in the z -direction, respectively. Δy is the fixed grid-cell size in the spanwise direction. Δt_f is the time step size

Table 2 Validation of the flow field solution

Re	Quantity	Present	Saha [36]	Absolute difference (%)
50	Str	0.15	0.15	0
	C_d	2.13	2.47	13.8
100	Str	0.19	0.18	5.6
	C_d	2.62	2.60	0.8

The term $(\frac{\partial u_f}{\partial z})_{x=0}$ in the above Eq. (7) is the local fluid velocity gradient at the domain inlet. The average flow Reynolds number (Re_{avg}) based on h and U_c can be defined as $Re_{\text{avg}} = U_c h / \nu_f$ and held fixed in all our studies at 60. The flow at such a moderately low Reynolds number is two-dimensional and demonstrates laminar vortex shedding characterized with a von Kármán vortex street on the downstream side of the plate. The details regarding the grid size and time step size are documented in Table 1. The current mesh in x direction is finer than that of Singh and Narasimhamurthy [33], where they performed DNS of a turbulent wake behind a normal flat plate. The chosen grid resolution is fine enough for running the present DNS simulations.

The boundary conditions imposed for solving the carrier flow are as follows: At the inflow, $u_f = U_c$ (uniform flow) or $u_f = K U_c$ (linear shear inflow); $v_f = w_f = 0$. Additionally, $\partial p / \partial x = 0$. At the outlet, we impose $\partial u_f / \partial x = \partial v_f / \partial x = \partial w_f / \partial x = 0$, and pressure p is set to zero. For side walls, periodic boundary conditions are imposed. Bottom and top walls are treated as free-slip walls by setting $w_f = 0$; $\partial u_f / \partial z = \partial v_f / \partial z = 0$ and $\partial p / \partial z = 0$. The plate surface is treated assuming a no-slip boundary condition.

For the validation of the setup and procedure used to obtain the carrier flow solution, two common quantities of engineering interests viz. Strouhal number (Str) and drag coefficient (C_d) are compared against DNS results of Saha [36]. Here, the former $Str = fh / U_c$ is a dimensionless frequency of the vortex shedding from the plate (f = frequency of vortices shed from the plate), while the latter $C_d = 2F_d / \rho_f U_c^2 b h$ is a dimensionless resistance of the plate to the carrier flow (F_d = time-averaged drag force; b = spanwise plate dimension). The absolute difference (in %) between present simulation results and reference data is also shown in Table 2. Our simulation results show a reasonable agreement with the reference data. The difference between the present simulation results and reference data could be due to the differences in the solution methodologies, numerical schemes, imposed boundary conditions, computation domain size, and mesh size.

3.2 Lagrangian particles

We start seeding tiny solid spherical particles in the domain after the periodic vortex shedding is established. Three different classes of particles are considered, wherein each particle class is characterized by the unique particle Stokes number (St). St is obtained by normalizing the particle relaxation time τ_p with the characteristic flow time scale, h / U_c . Properties of a particle for each class are shown in Table 3. We remark that the diameter of a particle d_p of any given class is significantly smaller than the hydrodynamic length scale h in the problem (i.e., $d_p \ll h$), allowing us to treat it as a point-particle. The maximum particle Reynolds number ($Re_{p,\text{max}}$) for each St-class in the uniform inflow case is also documented in Table 3. The maximum among instantaneous Re_p values of all the particles in the computational domain is averaged during a vortex shedding period to obtain $Re_{p,\text{max}}$. The particle-fluid hydrodynamic interaction is described as a one-way momentum coupling. Four particles are seeded at each time step for each class near the domain inlet at random cross-stream (z/h -) positions. Particles are seeded uniformly for the uniform inflow case. However, uniform and non-uniform

Table 3 Particle properties

Parameter	Class-1	Class-2	Class-3
St	0.1 (low)	1 (medium)	10 (high)
ρ_p/ρ_f	2000	2000	2000
d_p/h	3.9×10^{-3}	1.23×10^{-2}	3.87×10^{-2}
$Re_{p,max}$	0.1	0.51	2.4

particle seeding methods (i.e., two different sub-cases) are considered for the shear inflow case. In the non-uniform seeding case, the number of seed particles increases linearly in z -direction with the rate same as the local fluid velocity to ensure a constant mass flow rate. Initial particle velocity is set equal to the local fluid velocity. If any particle approaches the plate body such that its center is located within a distance equal to its radius from the body surface, then the particle is considered to be deposited on the body and removed from the simulation. In other words, we assume a perfect absorption condition between a particle and the contacting plate's surface. Further, any particle crossing the computation domain boundary is removed from the simulation. The selected particle seeding rate ensures that nearly 10^5 particles are present in the computational domain in uniform and shear inflow cases. Since MGLET-LaParT is a 3D solver, we do not make any two-dimensional simplification while solving particle phase equations (even if the distribution of particles is 2D).

4 Results and discussion

In this Section, results obtained from our simulation primarily focusing on the effects of the planar shear inflow on the dispersed phase transport and corresponding statistical quantities are discussed. We first discuss the deposition of particles on the plate. A comparison of instantaneous particle distribution observed in uniform inflow with shear inflow case is then discussed. The latter part of our discussion highlights how shear inflow influences particle dispersion statistics. In any comparative assessment between uniform and shear inflow cases, uniform particle seeding method can be assumed for each case if not specified explicitly. Dispersed phase results are reported after ensuring that the entire computation domain is completely occupied with particles in any given case. After the injection of particles in the computation domain, simulations are run for 90 and 180 h/U_c time duration for the uniform and shear inflow cases, respectively.

4.1 Particle deposition

Particles released near the inlet are transported downstream via the carrier flow. Of such particles being transported, a small fraction of particles that impact any face of the plate is considered deposited. In both uniform and shear inflow cases, we observe that a large proportion of such particles belonging to any given St-class deposits on the front face of the plate by the impaction mechanism. Particles rarely deposit on the side and lee faces at $Re=60$. The deposition efficiency of particles (η) for each St-class is documented in Table 4. Here, η is the fraction of particles (in %) deposited on the plate to the total number of particles approaching the plate through the projected area of the plate at the inlet. From Table 4, it is clear that η increases with particle Stokes number St in both uniform and shear inflow cases. Low St-class particles adapt to the local fluid motion quickly. Thus, a small fraction of seeded particles approaching the plate whose cross-stream positions are very close to the longitudinal centerline is deposited. The rest moves around the plate following the local fluid motion. On the contrary, the motion of high St-class particles is hardly affected by the local flow owing to their large inertia. A large fraction of such particles approaching the plate through its frontal projected area is deposited on the plate. The deposition behavior of the medium St-class particles is in between low and high St-classes. These qualitative observations for the uniform inflow case are consistent with previous studies on particle deposition over a square cylinder obstruction placed in the channel flow (see Brandon and Aggarwal [5], Afrouzi et al. [7], Bagheri and Sabzpooshani [9]). The presence of linear shear does not substantially affect particle deposition. Nevertheless, a marginal decrease in particle deposition efficiency is observed for high St-class (i.e., $St = 10$). The local flow field on the upstream side of the plate becomes a little asymmetric about the longitudinal centerline in the shear inflow case. Thus, trajectories of particles approaching the plate from its bottom side are slightly shifted away from the plate. In effect, more particles escape from the bottom side than the top, resulting in a slight reduction in the particle deposition efficiency, especially for high St-class. We

Table 4 Particle deposition efficiency (η)

St	Uniform inflow		Planar shear inflow: uniform particle seeding		Planar shear inflow: non-uniform particle seeding	
	η	RSD	η	RSD	η	RSD
0.1	0.3	10.7	0.3	8.3	0.3	6.4
1	59.0	0.3	58.4	0.5	58.9	0.2
10	96.8	0.2	96.1	0.3	95.3	0.2

η values documented here are averaged in time over $30 h/U_c$ duration after reaching a stationary state. Furthermore, the corresponding relative standard deviations (RSD) of η values (expressed in %) are also documented in the next column to represent the statistical noise. Here, RSD is the ratio of the standard deviation of η to its mean multiplied by 100

also provide supplementary videos to aid readers in visualizing the motion of particles of different St-classes in the vicinity of the plate for both cases.

4.2 Instantaneous particle distribution

Here, we discuss the shear inflow effect on the time evolution of the instantaneous distribution of particles. With this aim, the instantaneous distribution of representative medium St-class particles (i.e., $St = 1$) at different time instants during a vortex shedding period is shown in Fig. 3. The evolution of particle distribution in time with uniform inflow case (shown in instantaneous snapshots a–e) is compared against the linear shear inflow (f–j). Here, two successive snapshots are spaced apart by $T_s/4$ (uniform inflow case) or $T_u/4$ (shear inflow case) in time, where $T_u \approx 6h/U_c$ and $T_s \approx 6.2h/U_c$ are times required to complete one shedding cycle in uniform and shear inflow case, respectively. Contours of instantaneous spanwise fluid vorticity magnitude (color background) are also superimposed on the corresponding particle distributions in each snapshot. We specifically focus our attention on the von Kármán vortex street region formed downstream of the plate shown in snapshots of Fig. 3. It is evident here that the collective motion of particles is highly organized in both uniform and linear shear inflow cases, albeit particle distribution patterns are distinctly different. Particles are localized at the peripheral regions of vortices in both cases. The expulsion of particles from such regions of high vorticity magnitude leads to the formation of void regions, which are transported downstream alongside their encapsulating particle clusters. The instantaneous flow field and particle distribution pattern observed in the uniform inflow case qualitatively resemble those in previous studies performed on dilute particulate suspension flows over a circular cylinder (Zhou et al. [12], Shi et al. [14]). Nonetheless, a comparison of the present pattern with Zhou et al. [12] at the same $Re = 60$ also suggests a few notable qualitative differences (owing to the differences between the bluff-body geometry), which are worth highlighting. For instance, the first leaf-shaped (particle-depleted) void region forms relatively closer to the bluff-body in the present case than observed in Zhou et al. [12] since vortices are detached nearer to the body than the latter. As such void regions are transported further downstream to get a balloon-shaped appearance, adjacent void regions (having opposite orientations) are separated by a very thin dense cluster of particles in the present case (uniform inflow). On the contrary, adjacent void regions observed in Zhou et al. [12] are sufficiently spaced apart by a thick layer of particles. However, patterns observed in the shear inflow case have not been noticed in earlier studies and appear quite peculiar. The effect of shear in the inflow on void regions and peripheral particle clustering pattern is less appreciable in a region close to the plate on its downstream ($5 \leq x/h \leq 10$). This is understandable since the carrier flow topology in this region is not drastically modified due to the shear effect. As such particle-depleted void regions and peripheral particle clusters are transported further away from the plate in the downstream direction ($x/h \geq 10$), they undergo significant increases in their areas in both cases. In the uniform inflow case, we observe that positions of such void regions are streamwise staggered, and sizes of void regions located on either sides of longitudinal centerline but close to each other are not significantly different. In the shear inflow case, on the contrary, void regions located on the high-velocity side are much larger in sizes compared to nearby voids on the low-velocity side. Furthermore, the evolution of shapes of void regions during the transport in the shear inflow case is quite distinct from the uniform inflow. The progressive deformation and rotation of void regions during their transport in the shear inflow case are more pronounced than in the uniform inflow due to shear effects. In the uniform inflow case, void regions and peripheral particle clusters evolve from leaf-like shapes to balloon-like shapes while undergoing a slight rotation about the spanwise (y) axis. On the contrary, such regions are compressed in a cross-stream direction and stretched streamwise while subjected to a significant rotation to become oval in shapes in the shear inflow case. Such massive changes in

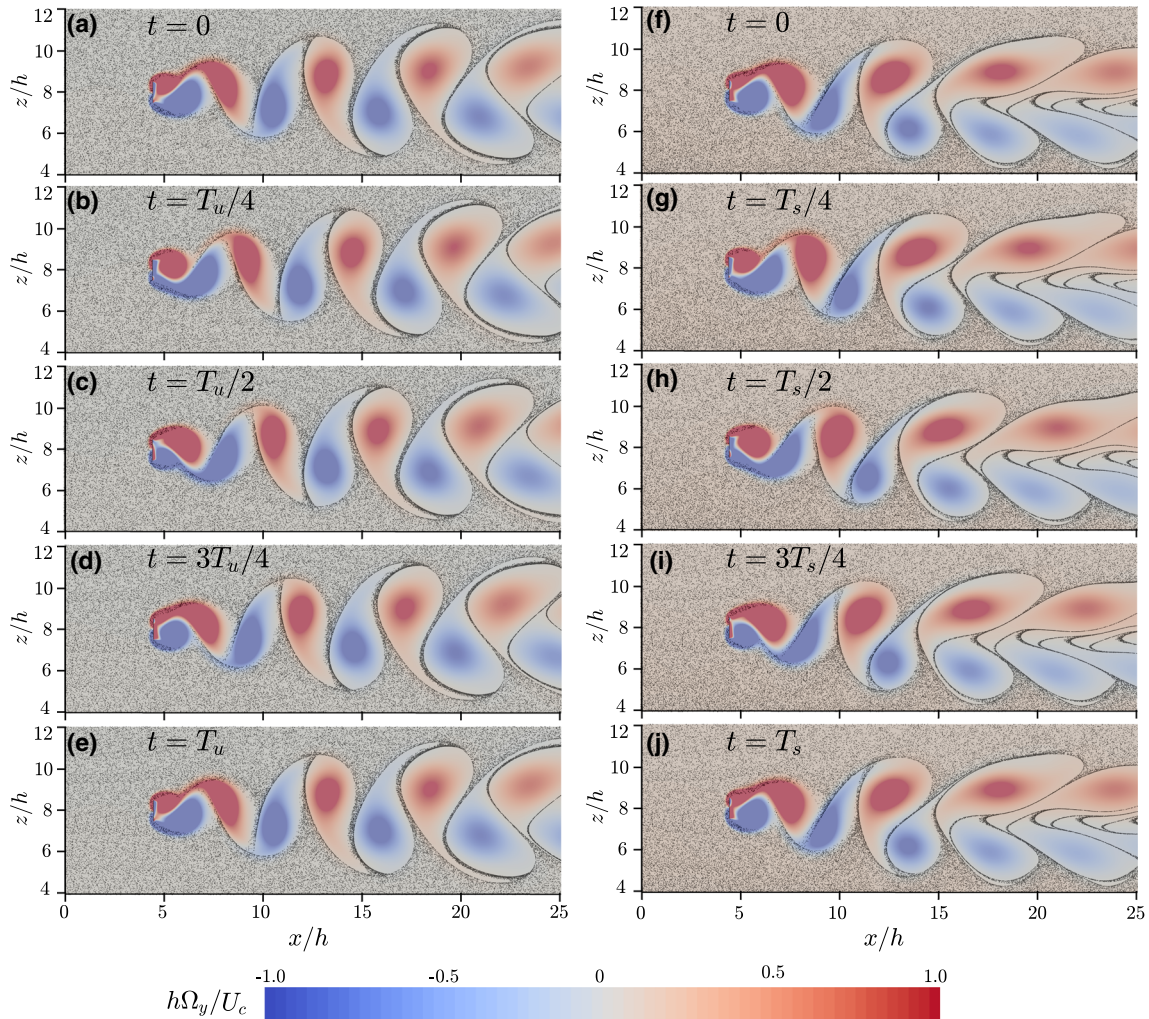


Fig. 3 Instantaneous snapshots of distribution of particles with Stokes number unity at five different time instants in a vortex shedding cycle: **a–e** uniform inflow, **f–j** planar shear inflow. Here T_u and T_s are vortex shedding periods for uniform and planar shear inflow cases, respectively. Particle distributions are superimposed over the spanwise vorticity $h\Omega_y/U_c$

the evolution of void regions and clusters of particles during their transport are dictated by similar changes in von Kármán vortices at corresponding regions caused by the shear effect. The massive stretching and rotation of clusters of particles formed at boundaries of vortices increase their concentration at regions located far away from the plate on its downstream side near the longitudinal centerline. Another remarkable observation from Fig. 3 is the displacement of void regions in the cross-stream direction toward the low-velocity stream, which suggests us that the dispersion of particles in the cross-stream direction is modified due to shear effects. The evolution of particle distribution in time in the non-uniform particle seeding sub-case with the shear inflow is quite similar to the uniform particle seeding and thus not shown here.

As seen in Fig. 3, medium St-class particles are non-uniformly distributed in the carrier flow, especially in von Kármán vortex street. To understand how shear affects the distribution of particles of different inertia, we explore the particle Stokes number (St) effect on their instantaneous distribution. For such a purpose, Voronoï analysis has emerged as a powerful tool to characterize and quantify the aforementioned non-uniform distribution of inertial particles [13, 14, 37–39]. Unlike the conventional tools to analyze the clustering of particles, we do not have to select an arbitrary length scale to construct a Voronoï diagram. This powerful feature of a Voronoï diagram makes it a more robust and flexible tool over the other conventional options (see Monchaux et al. [37] for a detailed discussion). We construct such Voronoï diagrams for analyzing the 2D distributions of particles (in the xz -plane) in the domain for different St-classes. For each diagram, the entire area of the computational domain projected on the xz -plane (i.e., $L_x \times L_z$) is partitioned into many Voronoï

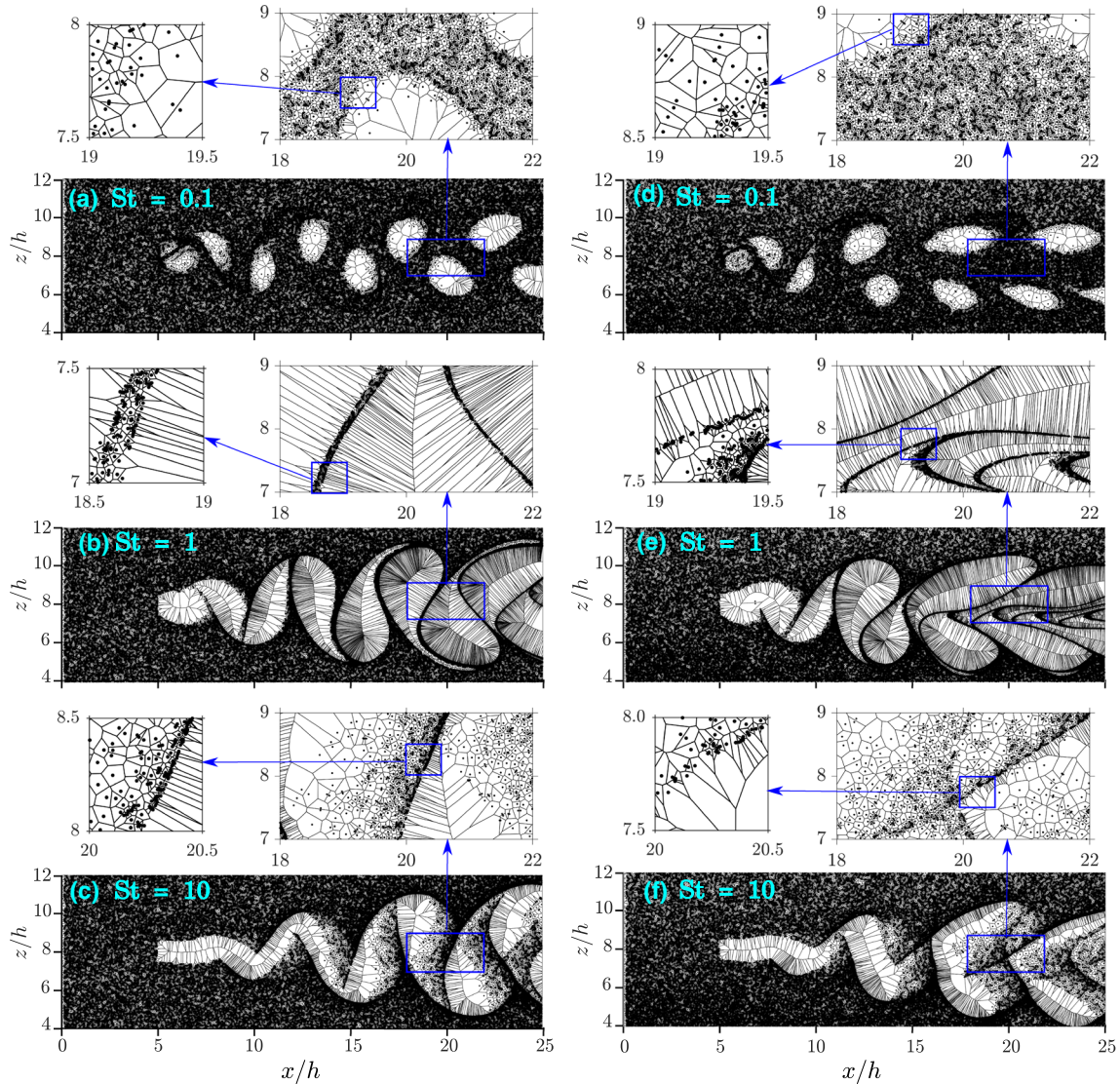


Fig. 4 Voronoi diagrams for instantaneous particles distribution: **a–c** uniform inflow, **d–f** planar shear inflow. Diagrams are shown for the three cases of particles Stokes numbers, viz., **a, d** $St = 0.1$, **b, e** $St = 1$, and **c, f** $St = 10$

cells (polygons). Each Voronoi cell corresponds to a unique particle such that its area is inversely proportional to the local particle concentration. In Fig. 4, Voronoi diagrams to characterize the distribution of particles of different St values for both uniform and planar shear inflow cases are shown. The magnified views of the interface between dense and less dense particle concentrations are also shown in panels above each of the Subfigures (a–f). Mutually connected Voronoi cells having visibly large areas locally forming groups on either sides of the longitudinal centerline—suggesting particle-depleted void regions—could be easily identified for each particle class. The non-uniformity in distribution of areas of Voronoi cells for particles of $St = 1$, and 10 is evident indicating significant in-homogeneity in local particle distribution. The stretching and rotation of particle-depleted void regions and peripheral particle clusters in shear inflow case are substantially large compared with uniform inflow for all particle classes. Thus, local particle concentration away from the plate on its downstream ($x/h \geq 10$) is influenced due to shear effects in all the cases. The presence of shear in the inflow impacts differently on each St -class of particles.

- During the transport of low St -class particles, the streamwise positions of particle-depleted void regions formed on either side of the wake centerline are staggered in the uniform inflow case. On the contrary,

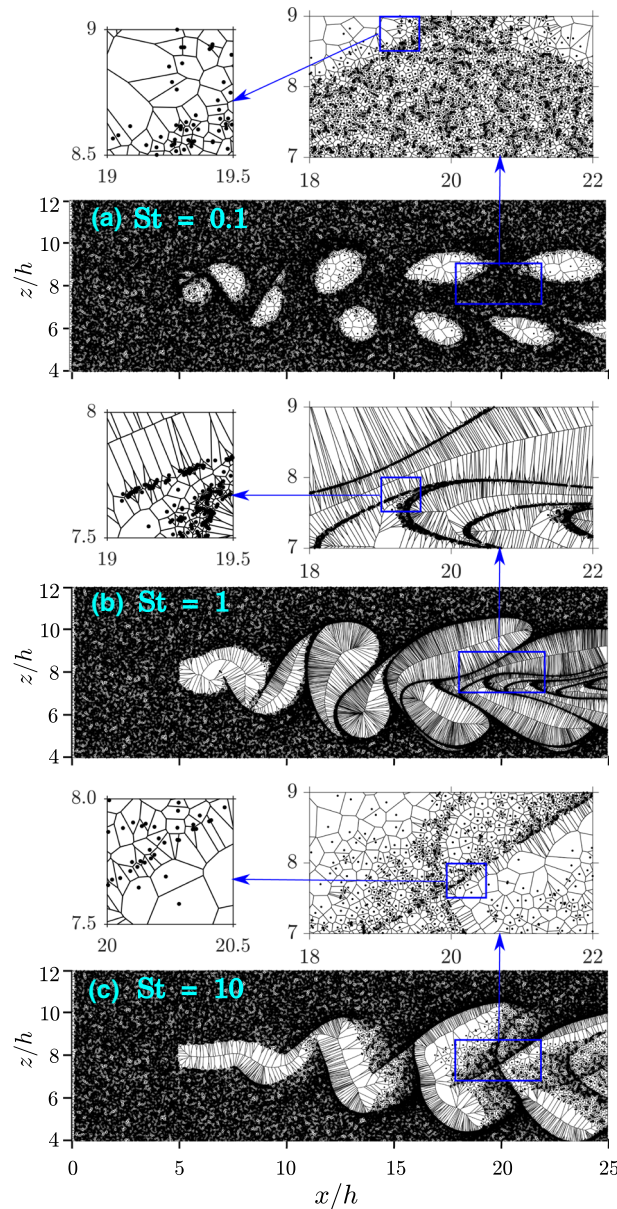


Fig. 5 Voronoi diagrams for instantaneous particles distribution for the planar shear inflow with the non-uniform particle seeding. Diagrams are shown for the three cases of particles Stokes numbers, viz., **a** $St=0.1$, **b** $St=1$, and **c** $St=10$

such a staggered arrangement is disturbed in the shear inflow case due to shear effects. Furthermore, shear in the inflow also increases the spacing between void regions formed on either side of the wake centerline.

- The impact of shear on the distribution and local concentration of particles is maximum for the medium St -class among all the particle classes. The effect of shear on transport of medium St -class particles causes nearby void regions to remain in proximity on their upstream sides while opposite ends to spread away from each other in the cross-stream direction.
- The transport of high St -class particles is characterized by a behavior similar to the medium St -class, but with the exception that void regions from either side of the longitudinal symmetry axis merge into one another.

Unlike the uniform flow case, the transport of particle-depleted void regions with the shear inflow is not symmetric about the longitudinal symmetry axis for all the three St -classes. Such void regions while being transported downstream progressively shift laterally toward the low-velocity side of the flow. The shift is

large for particle of Stokes numbers (St) 1 and 10. Voronoï diagrams are also shown separately in Fig. 5 for different St-classes of particles for the planar shear inflow and non-uniform particle seeding. The alikeness of these diagrams with ones shown for uniform particle seeding (Fig. 4d–f) suggests that the method of particle seeding does not affect the qualitative distribution of particles of any given St-class. However, Voronoï cells' sizes increase in z -direction in the uniform particle seeding sub-case; they do not vary in the corresponding direction in the non-uniform particle seeding sub-case.

4.3 Particle dispersion statistics

The effect of shear inflow on dispersion statistics of three different St-classes of particles is explored here. All the statistical quantities vary along x - and z -directions. They are obtained by time-averaging instantaneous samples. Statistical samples are recorded for nearly eight vortex shedding cycles, where two consecutive samples are separated by $0.01h/U_c$ in time. The frontal area of the computational domain ($L_x \times L_z$) is partitioned into a $2D$ mesh comprising many rectangular elements to calculate the particle dispersion statistics. The statistical mesh uses 125 streamwise divisions of uniform thicknesses (in domain length) and 200 cross-stream divisions of equal heights (in domain height). It is ensured that reported statistics are not sensitive to chosen numbers of slabs and blocks. We compare cross-stream (z -) profiles of particle dispersion statistics obtained in the uniform inflow against the linear shear inflow (with the uniform particle seeding) at five chosen streamwise positions: $x/h = 4.5$ (near the plate on its upstream side); $x/h = 5.5$, and 7.1 (near the plate on its lee side); $x/h = 14.5$, and 22.5 (away from the plate on its downstream side). Note that the standard deviations (σ) are represented using error bars superimposed over the cross-stream profile of a statistical quantity. The length of each error bar is 2σ . The variation of mean particle concentration (C/C_{avg}) in the z -direction is shown at various streamwise positions (x/h) in Fig. 6. For obtaining mean normalized particle concentration (C/C_{avg}), first, the average number of particles within a mesh element is divided by the area of the element to obtain local average particle concentration C . C is then further divided by average particle concentration in all the elements, C_{avg} to estimate C/C_{avg} . It is evident from Fig. 6 that the shear inflow in conjunction with uniform random seeding of particles causes the mean particle concentration to increase from the high-speed to low-speed stream region. On the contrary, there is no such global mean particle concentration gradient in the cross-stream direction in the uniform inflow case. The influence of shear on mean particle concentration is not significant at streamwise positions near the plate. However, significant changes are observed in the mean particle concentrations for all St-classes at farther downstream positions from the plate (i.e., $x/h = 14.5$, and 22.5). To understand such modifications, it is convenient to focus on one of such streamwise positions for the ease of comparative assessment. To this aim, we fix our attention at the farthest downstream position from the plate ($x/h = 22.5$). For low St-class particles, it is noticed that the lateral extent of high particle concentration region is increased in the shear inflow case near the longitudinal centerline. Nonetheless, changes in concentration of such low inertia particles are less substantial. However, for medium St-class particles, we observe that two local peaks symmetrically positioned on either side of the longitudinal centerline in the uniform inflow case have diminished in the shear inflow. Both diminished peaks in the latter case show a lateral shift toward the slow-stream side. This is due to the lateral displacement of von Kármán vortices in the shear inflow case, which causes the adjacent dense particle clusters to shift toward the slow-stream side. Furthermore, the diminished peak observed in the shear inflow case in the low-speed stream region is larger than in the high-speed region. This may appear a bit counter-intuitive at first sight since the strengths and sizes of counter-clockwise vortices in the low-speed region are lower than clockwise vortices in the high-speed region. However, it becomes comprehensible after noting that the availability of a large number of particles on the low-speed side facilitates augmenting the local peak concentration. A remarkable effect of shear for medium St-class particles is the formation of the high particle concentration region close to the wake centerline. This effect is due to the streamwise stretching of von Kármán vortices and peripheral thin dense clusters of medium St-class particles in the shear inflow case discussed in Sect. 4.2. We do not observe significant quantitative changes in particle concentration near the wake centerline in case of high St-class particles since their distribution is less affected (owing to their sluggish response) by such changes in vortical structures. However, the lateral shift in the positions of peaks in concentration profile toward low-speed stream is observed similar to the medium St-class, where the peak on the low-speed side is larger than at high-speed side due to the reasons discussed recently. Overall, the influence of shear to bring changes in mean particle concentration is maximum for medium St-class (i.e., $St = 1$) particles. In Fig. 6, we have also included C/C_{avg} profiles for the non-uniform particle seeding sub-case (see Fig. 6c). The mean particle concentration gradient observed in the domain for the uniform particle seeding sub-case

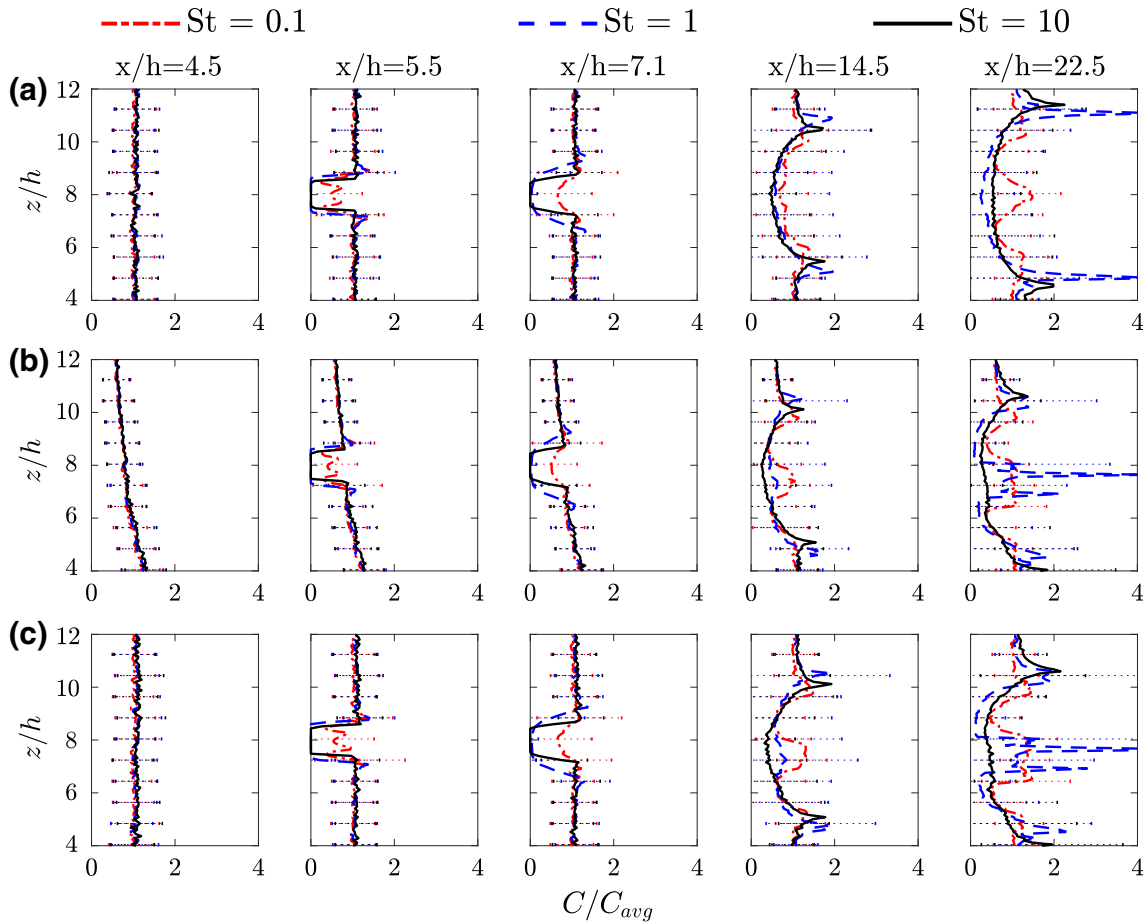


Fig. 6 Cross-stream profiles of mean normalized particle concentration (C/C_{avg}): **a** uniform inflow, **b** planar shear inflow with uniform particle seeding, **c** planar shear inflow with non-uniform particle seeding. Profiles are shown for particles of three different Stokes numbers (St), viz., 0.1, 1, and 10 at five different x/h positions

(see Fig. 6b) is absent for the non-uniform particle seeding (see Fig. 6c). Such profiles in both sub-cases are qualitatively similar for any given St -class of particles, irrespective of the nature of the particle seeding. However, quantitative differences are observed in profiles between the two sub-cases at streamwise positions far downstream from the plate ($x/h = 14.5$, and 22.5), especially for the medium and high St -class particles. A remarkable observation is that two local peaks of unequal magnitudes in the C/C_{avg} profile positioned on either side of the wake centerline in the uniform seeding sub-case become comparable in the non-uniform seeding sub-case.

In Fig. 7, cross-stream profiles of mean Voronoi cell area normalized using its average value (i.e., A^+) in the domain are shown. A Voronoi cell area (A^+) represents the reciprocal of the local particle concentration, and thus, the shear effect on the concentration of particles can be visualized in a different form here with similar observations discussed recently.

The effect of shear on the mean particle velocity (normalized with average inflow velocity, U_c) components is shown in Fig. 8 for all St -classes. Cross-stream profiles of streamwise (U_p/U_c) and cross-stream (W_p/U_c) components of the normalized mean particle velocity (shown in Fig. 8a, c, respectively) in the uniform inflow case are compared with corresponding profiles in the planar shear inflow (Fig. 8b, d). We first look at profiles of velocity components for the uniform inflow case (Fig. 8a, c). Here, streamwise velocities (U_p) of low and medium St -classes of particles approaching the plate (i.e., $x/h = 4.5$) are decreased, while cross-stream velocities (W_p) are increased. When some of such particles, which are not deposited on the plate, travel further in the streamwise direction from $x/h = 5.5$ to 7.1 (in the region where vortices remain attached), appreciable changes in their velocity components are observed. Here, the behavior of small St -class particles in the near-wake region is worth highlighting. When low St -class particles traveling closely around the plate reach the

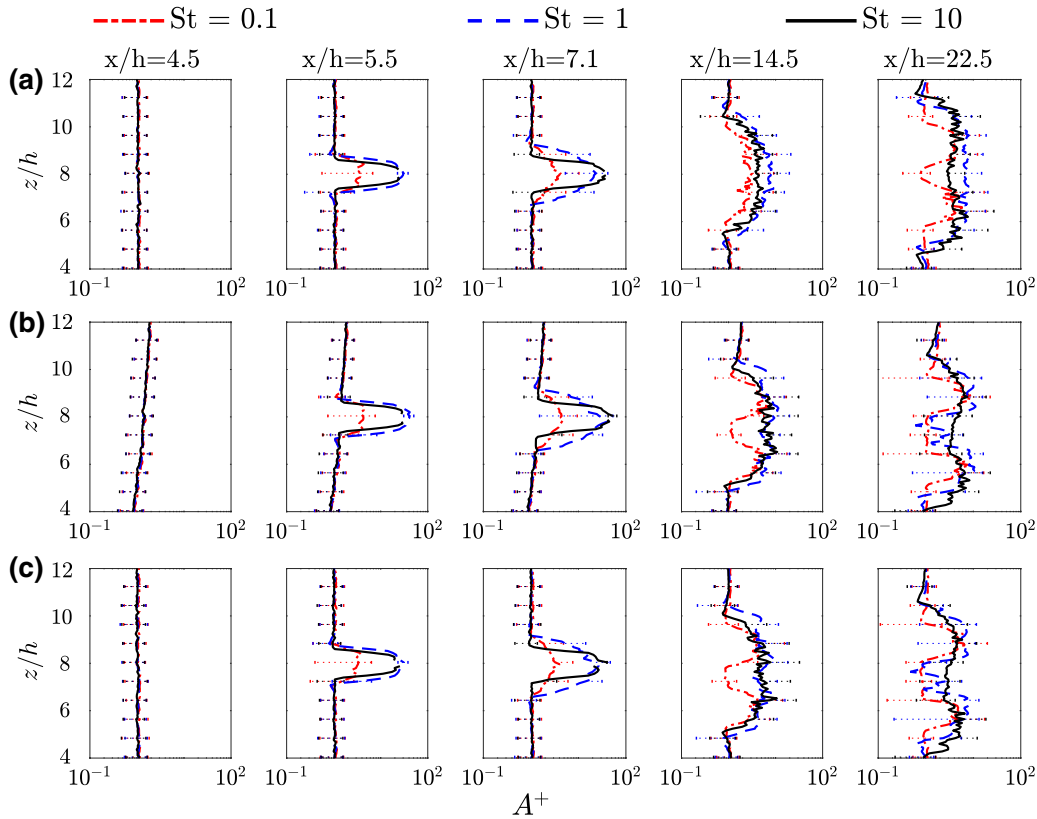


Fig. 7 Cross-stream profiles of mean normalized Voronoi cell area (A^+): **a** uniform inflow, **b** planar shear inflow with uniform particle seeding, **c** planar shear inflow with non-uniform particle seeding. Here, normalized mean Voronoi cell area A^+ is expressed as $A^+ = AN_p/(L_x L_z)$. Profiles are shown for particles of three different St, viz., 0.1, 1, and 10 at five different x/h positions

peripheral region of a growing vortex attached to the plate, they are brought inward into the wake region of the plate. Such particles get trapped between two oppositely rotating vortices attached to the plate. Some of the trapped particles approach the plate due to their negative streamwise velocity (i.e., $x/h = 5.5$). However, particles traveling around the attached vortex that has grown are not trapped since the grown vortex is pushed downstream by the opposite vortex. Such particles are ejected in the cross-stream direction, but their streamwise velocities are decreased (i.e., $x/h = 7.1$). Medium St-class particles also show similar behavior in the wake region at $x/h = 7.1$. However, the motion of particles from the high St-class appears to be ballistic (St=10) without significant changes in their velocities. Furthermore, such particles have an insignificant cross-stream velocity at any streamwise position. It is worth mentioning that high St-class particles close to the longitudinal centerline travel faster than low and medium St-class particles at streamwise positions far away from the plate. This behavior is due to the fact that the peripheral regions of von Kármán vortices located away from the wake centerline travel much faster than near ones. Since the motion of low and medium St-class particles is strongly coupled to von Kármán vortices, their streamwise momentum is retarded as they approach near the wake centerline during their cross-stream movement. On the contrary, the streamwise momentum of sluggish high St-class particles is hardly decreased. While taking a comparative look, we observe that the streamwise component of the mean particle velocity, U_p , increases in the cross-stream (z -) direction due to the shear in the inflow (Fig. 8a, b). It is worth noting that the shear has a modest effect on the cross-stream particle velocity, W_p (Fig. 8c, d). The shear impacts the streamwise particle velocity away from the plate on its downstream side (i.e., $x/h = 14.5$, and 22.5). The position of the local minima in streamwise velocity observed at the centerline in the uniform inflow case is shifted in the cross-stream direction further toward the low-speed stream in the shear inflow. The shift is again due to the cross-stream displacement of von Kármán vortices and adjacent particle clusters due to shear effects.

The drag force acting on a particle is directly dependent on the particle slip velocity, and thus, we explore the statistical behavior of particle slip velocity and discuss how it is influenced due to the shear in the inflow. We obtain such mean particle slip velocity (ΔU) by averaging the instantaneous particle slip velocity $\Delta \mathbf{u} = \mathbf{u}_f - \mathbf{u}_p$

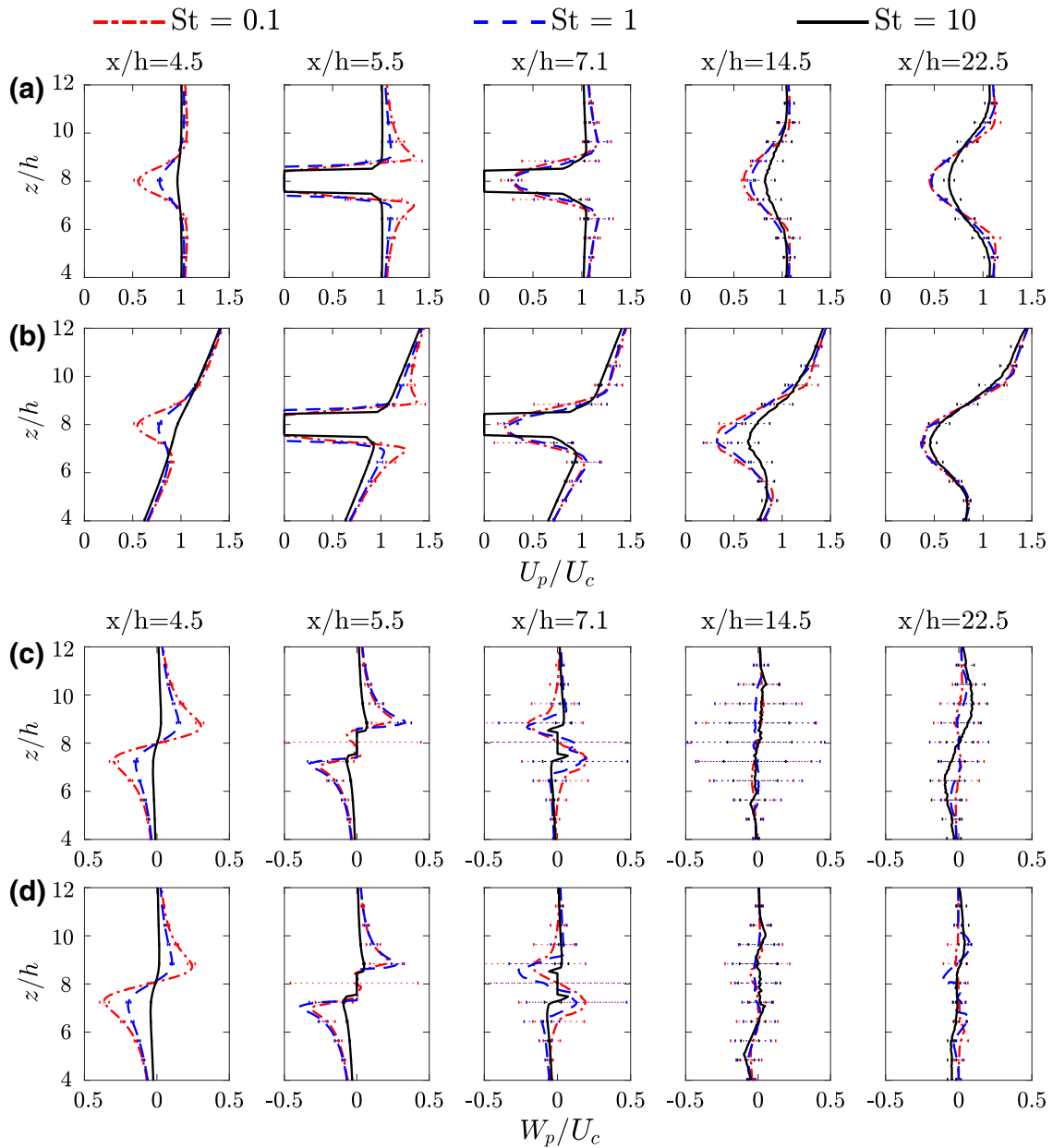


Fig. 8 Mean particle velocity cross-stream profiles: **a, c** uniform inflow, **b, d** planar shear inflow. **a, b** Streamwise component (U_p). **c, d** Cross-stream component (W_p). Profiles are shown for three different particle Stokes numbers (St) 0.1, 1, and 10

in time, where \mathbf{u}_f and \mathbf{u}_p are instantaneous local fluid and particle velocities, respectively. Thus, negative slip velocity suggests that particles travel faster than the local fluid and vice-versa. The effect of shear in the inflow on mean particle slip velocity cross-stream profiles is shown for all three particle classes in Fig. 9. We first focus on the uniform inflow case profiles (Fig. 9a, c). In general, it is observed that low St -class particles ($St=0.1$) mimic the local fluid motion, and thus, their slip velocities (ΔU and ΔW) are insignificant. On the contrary, magnitudes of slip velocities (ΔU and ΔW) of medium and high St -class particles increase significantly with an increase in St from 1 to 10. Depending on their streamwise positions, such particles travel faster or slower than the local fluid near the plate. For instance, such particles approaching the plate from its upstream side ($x/h=4.5$) travel faster than the local fluid in the streamwise direction ($\Delta U < 0$) but lag behind the latter in the cross-stream direction ($\Delta W > 0$). The motion of such particles further downstream but close to the plate ($x/h=5.5$, and 7.1) is characterized with drastic changes in both components of their slip velocity.

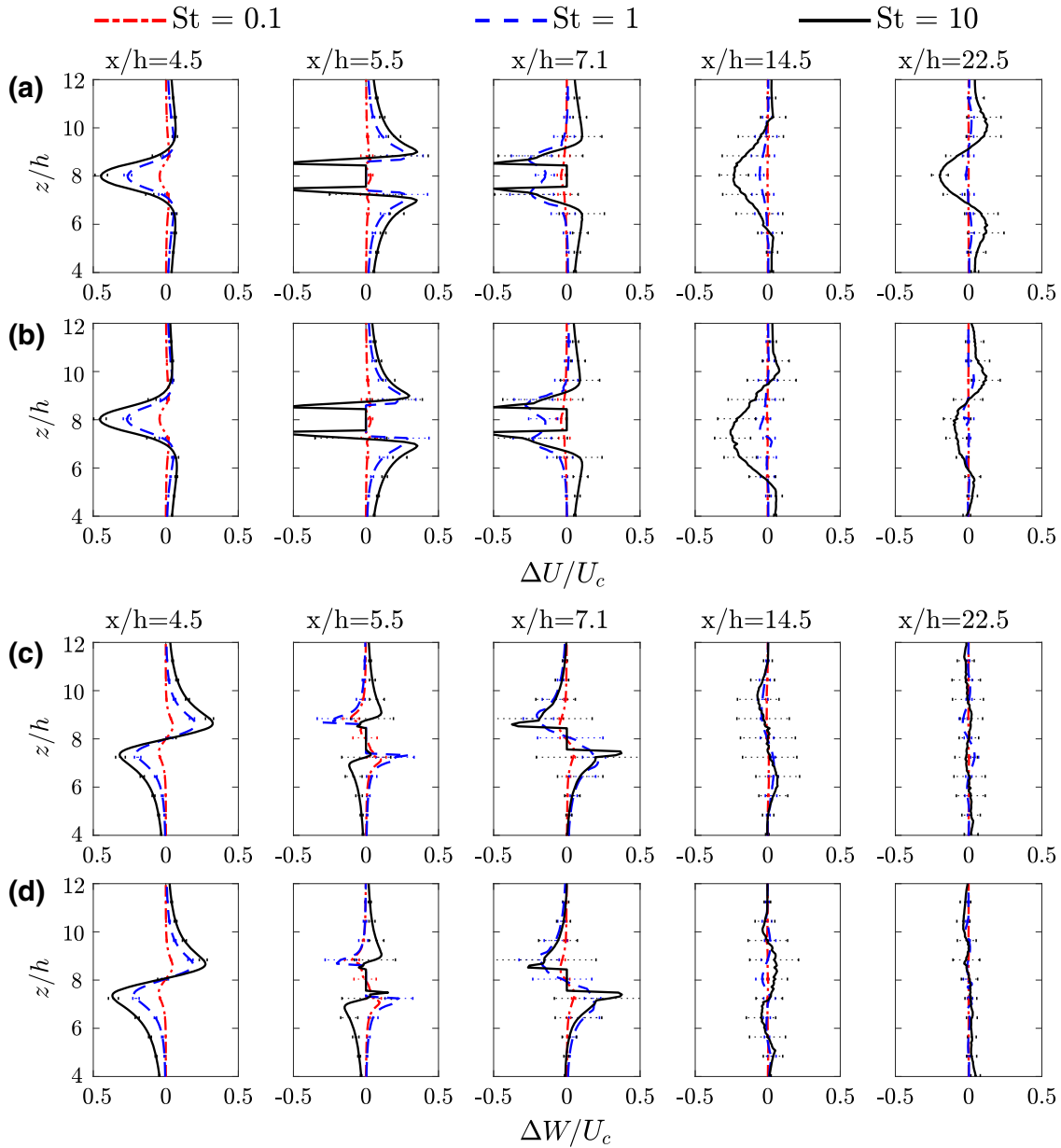


Fig. 9 Cross-stream profiles of mean particle slip velocity: **a, c** uniform inflow, **b, d** planar shear inflow. **a, b** Streamwise component (ΔU). **c, d** Cross-stream component (ΔW). Profiles are shown for three different particle Stokes number (St) cases, viz., 0.1, 1, and 10

As they travel further downstream in the vortex street (i.e., $x/h=14.5$, and 22.5), their mean streamwise slip velocities change but no significant changes in the cross-stream component are observed. Especially, the streamwise motion of medium and high St -class particles traveling near the longitudinal centerline is faster than the local fluid. While taking a comparative look to understand the overall effect of shear, we observe that profiles of the mean particle slip velocities at streamwise positions near the plate ($x/h=4.5$, 5.5 , and 7.1) are not impacted drastically due to shear. However, at streamwise positions away from the plate ($x/h=14.5$, and 22.5), shear in the inflow affects the mean streamwise particle slip velocity (ΔU), where regions with $\Delta U < 0$ show a considerable shift in their positions along the cross-stream direction from the longitudinal centerline (Fig. 9a) toward the low-stream side (Fig. 9b). This is understandable since similar lateral shifts are observed in vortices and particle clusters at corresponding regions due to the shear effect. However, we do not observe any substantial change in the corresponding cross-stream component (ΔW).

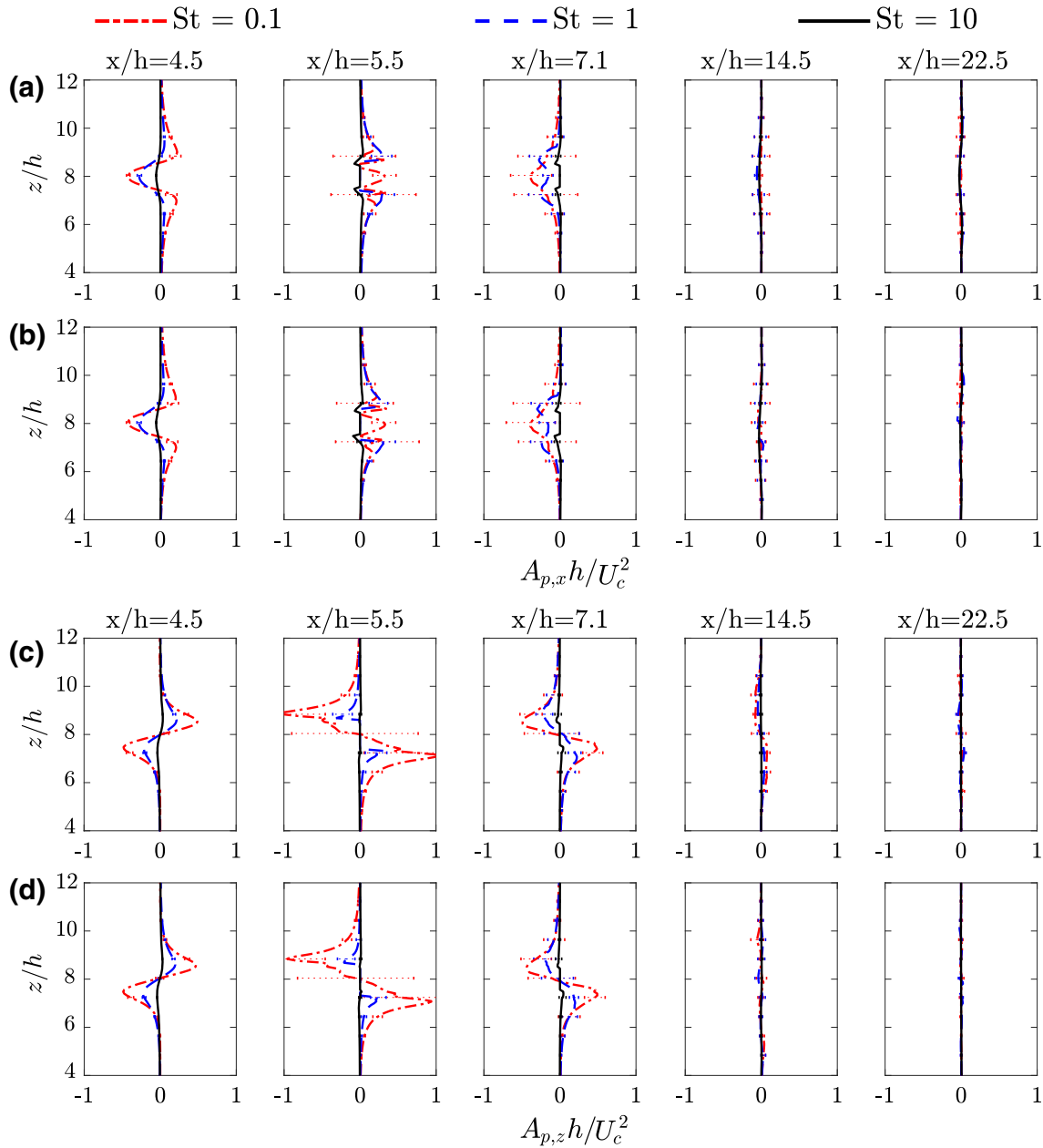


Fig. 10 Cross-stream profiles of normalized mean particle acceleration: **a, c** uniform inflow, **b, d** planar shear inflow. **a, b** Streamwise component ($A_{p,x}h/U_c^2$). **c, d** Cross-stream component ($A_{p,z}h/U_c^2$). Profiles are shown for three different particle Stokes numbers (St), viz., 0.1, 1, and 10

To gain further knowledge about the dynamics of particle motion, we also explore the statistics of particle acceleration at different critical streamwise positions in Fig. 10. Here, comparisons of mean streamwise $A_{p,x}$, and cross-stream $A_{p,z}$ particle accelerations profiles between uniform (Fig. 10a, c), and shear inflow (Fig. 10b, d) cases are shown. In both cases, particle motion is characterized by a substantial acceleration and deceleration at streamwise positions near the plate. It is observed that particles first accelerate while traveling over and below the plate ($x/h = 4.5$) but decelerate after entering the wake region ($x/h = 7.1$). When such particles reach streamwise positions far away from the plate, they do not have significant acceleration ($x/h = 14.5$ and 22.5). A comparison of profiles between uniform and shear inflow cases suggests no substantial effect of the shear in the inflow on the statistics of streamwise and cross-stream particle acceleration.

We remark that the particle velocity, slip velocity, and acceleration statistics for the uniform and non-uniform seeding sub-cases are the same. Therefore, the profiles for the planar shear inflow with non-uniform particle seeding are not included in the corresponding Figures.

5 Concluding remarks

In this paper, we have studied the effect of shear in the inflow on the dispersion of tiny inertial particles and their deposition over a normal flat plate. A hybrid Eulerian–Lagrangian framework is adopted to solve the laminar flow of dilute particulate suspension over the plate. All simulations are performed using a newly developed solver MGLET-LaParT, and numerical methodology implemented in the solver is discussed in detail. The effect of shear in the inflow is assessed by directly comparing uniform inflow and planar shear inflow cases. Particles are seeded uniformly across the computation domain inlet for the former. In contrast, uniform and non-uniform particle seeding methods have been used separately in two different sub-cases for the latter. The shear parameter K for the latter case is limited to 0.1. The flow Reynolds number Re_{avg} based on the average inflow velocity is fixed at 60 in both cases. At such a low Reynolds number, the carrier flow demonstrates a periodic von Kármán vortex street in the wake from the plate. Particles of three different classes are considered for each set of the above simulations, where each distinct particle class is represented by its unique Stokes number (St), viz., 0.1 (low St -class), 1 (medium St -class), and 10 (high St -class). We observe that the evolution of shapes and sizes of von Kármán vortices shed from the plate is affected due to the shear effects. Such changes in the flow topology result in a significant deformation and rotation of particle-depleted void regions and adjacent particle clusters at corresponding regions. Some key findings from the present study can be summarized as follows:

- (i) The presence of linear shear in the approach flow causes a marginal reduction in deposition efficiency of high St -class particles ($St = 10$).
- (ii) For the shear inflow with the uniform particle seeding, an intuitive effect of shear that directly affects the dispersed phase transport is that the population of slow-moving particles is more significant than of faster particles. Overall, there is a mean particle concentration gradient in the domain whose direction is opposite to the inflow velocity gradient. However, such a mean particle concentration gradient does not exist for the non-uniform particle seeding.
- (iii) We find that shear in the inflow, albeit characterized with a moderate shear parameter ($K = 0.1$), significantly changes distribution and dispersion of particles, especially at streamwise positions away from the plate. Such changes are triggered by streamwise stretching and rotation of particle-depleted void regions and adjacent particle clusters during their downstream transport away from the plate. Furthermore, such void regions and particle clusters shift toward low-stream regions due to shear effects. The extent of such lateral shift increases with St from 0.1 to 10. The qualitative distribution of particles in the shear inflow case is not influenced by the choice of the particle seeding method.
- (iv) The impact of shear on the local mean concentration of particles is dependent on their inertia (St). A dramatic impact is observed on medium St -class particles (i.e., $St = 1$). This is evident from the shift in peak mean particle concentration regions located away from the longitudinal centerline (on either side) to the centerline region.
- (v) The effect of shear on particle velocity statistics (e.g., U_p and W_p ; ΔU and ΔW) is not noticeable at streamwise positions near the plate. However, quantitative changes in the profiles are evident at streamwise positions far away from the plate. A remarkable observation at any such position is that the local minima observed U_p or ΔU profiles shift appreciably toward the low-speed stream from the centerline. However, we do not find any substantial effect of shear on the particle acceleration statistics.
- (vi) The choice of particle seeding method (i.e., uniform/non-uniform) in the shear inflow case leads to quantitative differences in the concentration profiles of the medium and high St -class particles. Such quantitative differences in the velocity and acceleration statistics are not observed.

The above findings suggest that even a modest shear in the approaching flow could substantially impact the dispersed phase transport. The current outcome may find application in particle segregation and collection.

The methodology used in this study can be extended to study turbulent flows of particulate suspension. If a turbulence model is used (instead of DNS) to solve the carrier flow, then additional models for particle dispersion are needed. The feedback from the particle phase to the fluid (i.e., two-way coupling) will be taken into account in future to solve flow with a large volume fraction and mass loading of the dispersed phase. The particle deposition model used in the present study can be extended to a deposition-collision model that

would account for the probability of a particle rebound in addition to the deposition. Such a particle deposition-collision model will have to consider the additional factors, such as the contact force (e.g., van der Waals force), friction force, and material elastic behavior properties (see Bouris et al. [40], Tong et al. [41]). The present methodology can be extended to study particles relatively lighter than the ones considered in the present study (i.e., particle-to-fluid density ratio $(\rho_p/\rho_f) \leq O(10)$) by including the additional forces, such as added-mass and Basset history in the equation of particle motion.

Acknowledgements The authors thank Yucheng Jie, Department of Engineering Mechanics, Tsinghua University, China, for his help regarding the Voronoï analysis and sharing the relevant scripts.

Appendix A: LaParT details

See Fig. 11.

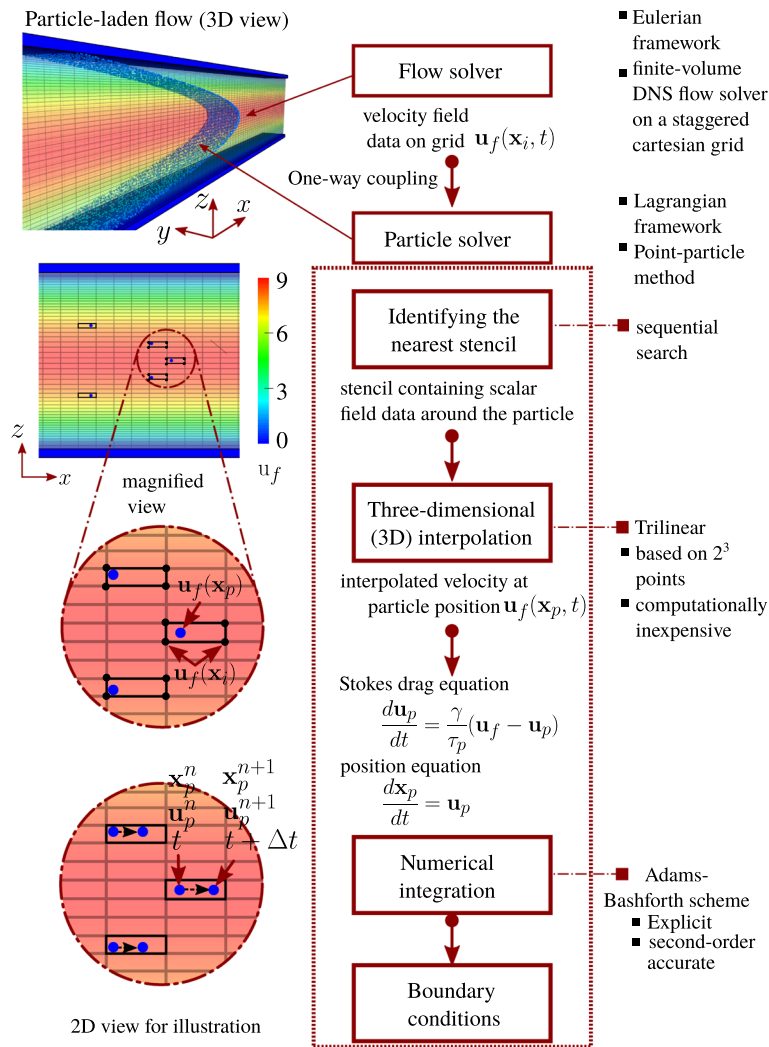


Fig. 11 Algorithm for the proposed Eulerian-Lagrangian solver MGLET-LaParT

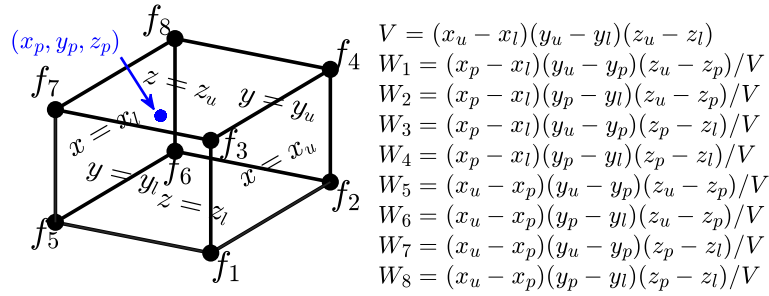


Fig. 12 Stencil for trilinear interpolation

1. Identifying the nearest stencil (neighbor search)

The first step in the algorithm is to identify the appropriate stencil (containing the velocity component data and their corresponding positions) encapsulating a particle for each velocity component. We again emphasize that the positions used to compute and store the velocity component field (i.e., u_f , v_f , and w_f) are staggered in relation to those for the pressure field (p) in the respective directions (i.e., x , y , and z). The sequential search method is used to identify the host stencil.

2. Three-dimensional (3D) interpolation

We obtain the fluid velocity ($\mathbf{u}_f(\mathbf{x}_p, t)$) at the particle position (\mathbf{x}_p) by interpolating the velocity field data available at nodes of the identified stencil. The choice of the interpolation scheme is important since it affects the accuracy of numerically computed particle variables (e.g., particle trajectory) and the computation cost. We expect that the interpolation scheme should be at least second-order accurate.⁷ The scheme should be easy to implement and affordable in terms of computational cost. Thus, we have implemented the trilinear interpolation based on 2^3 points [42] in the LaParT.

The interpolated value $g^{TL}(x_p, y_p, z_p)$ is constructed from scalar values (i.e., u_f , v_f , and w_f) located at 2^3 grid nodes at any interior position (x_p, y_p, z_p) within a rectangular 3D stencil. This stencil is formed by a bounding pair of constant x -, y -, and z -planes in each direction as shown in Fig. 12. The interpolated value $g^{TL}(x_p, y_p, z_p)$ by making use of the trilinear scheme is given as

$$g^{TL}(x_p, y_p, z_p) = \sum_{i=1}^8 W_i f_i \quad (8)$$

where the index of the corner point i varies from 1 to 8, f_i is the scalar value at the corner point, and W_i is its corresponding weight used in the interpolation (shown in Fig. 12). This scheme is computationally inexpensive and second-order accurate.

Here, we bring to the reader's attention that the velocity component is interpolated independently of the other components for any interpolation scheme. In other words, the incompressibility of the velocity field is not enforced in the interpolation scheme. This non-conservative nature of the interpolation can induce the non-physical clustering of particles due to numerical artifacts (see [16,43]). Nevertheless, we use a fine grid resolution to minimize such effects.

3. Numerical integration

An explicit second-order Adams–Bashforth scheme is used to integrate Eq. (5) numerically. Particle velocity at the new, i.e., $(n+1)^{th}$ time step by making use of Adams–Bashforth scheme is given using Eq. (9). Here, the solution at the first time step is computed using the first-order Euler's scheme,

$$\mathbf{u}_p^{n+1} = \mathbf{u}_p^n + \frac{\gamma \Delta t_p}{\tau_p} \left[\frac{3}{2}(\mathbf{u}_f^n - \mathbf{u}_p^n) - \frac{1}{2}(\mathbf{u}_f^{n-1} - \mathbf{u}_p^{n-1}) \right]. \quad (9)$$

⁷ This requirement is due to the fact that the present Eulerian solver MGLET uses spatially second-order accurate discretization schemes to compute fluxes.

The particle position is updated according to Eq. (10) as

$$\mathbf{x}_p^{n+1} = \mathbf{x}_p^n + \Delta t_p \left[\frac{3}{2} \mathbf{u}_p^{n+1} - \frac{1}{2} \mathbf{u}_p^n \right]. \quad (10)$$

The scheme is conditionally stable. We can not exactly estimate the Δt_p value to ensure that the numerical integration of Eqs. (5) and (6) is stable since these equations contain a term $\mathbf{u}_f(\mathbf{x}_p, t)$, which is not known a priori (see [44]). Jacobs et al. [45] mention that an approximate value of Δt_p (for stable numerical integration) can be given by

$$\Delta t_p < \sigma_p \tau_p \quad (11)$$

where the constant σ_p is equal to unity. Using Eq. (11), the value of Δt_p can be selected according to the τ_p value. However, as noted by Kontomaris et al. [46], Δt_f required to satisfy the CFL criterion to solve the carrier phase equations is lower than Δt_p required for the stable computation of the dispersed phase equations. We use the same time step size value for both the carrier and dispersed phase (i.e., $\Delta t_f = \Delta t_p$) in turbulent flow simulations. This conservative approach leads to a Δt_p value which is at least one order of magnitude smaller than the particle relaxation time τ_p and, thus, sufficiently small for the stable computation of the dispersed phase equations.

Regarding the boundary condition, if any particle approaches the body or a domain boundary, then an appropriate boundary condition is applied. For instance, if any particle crosses the boundary of the computation domain, then it would not be tracked further for the computation.

Appendix B: Verification and validation

1. Verification of LaParT

The verification of the numerical accuracy of schemes implemented in the Lagrangian solver using canonical numerical tests is discussed in test cases 1.1 and 1.2. The Lagrangian solver is isolated from the Eulerian solver, and numerical tests are performed on the former. The carrier phase velocity field (described using analytical expressions) is directly assigned to the Eulerian grid nodes without solving the Navier–Stokes equations. The motion of a particle in such tests can be determined analytically. Therefore, a direct comparison between numerical and analytical solutions can be made to quantify the numerical errors associated with any scheme. In the verification test 1.3, the carrier and dispersed phases are solved using MGLT-LaParT.

1.1. Particle in a steady sinusoidal flow

We track an inertia-free particle in a steady 2D sinusoidal flow (in xz -plane). This test problem is the same as that used by Marchioli et al. [27] to verify the order of accuracy of the interpolation based on the Taylor-series expansion. Prior to them, Kontomaris et al. [46] also had used the present problem for testing various interpolation schemes. The purpose of this test is to quantify the errors associated with an interpolation scheme and confirm its order of accuracy. The sinusoidal velocity field in this problem is described by $u_f = A_1$ and $w_f = A_2 \sin(k_x x)$ (in m/s) where $A_1 = A_2 = 0.025$ are constants (in m/s) and $k_x = \pi$ is the wavenumber. The particle is located at $x_p(0) = -0.8$ and $z_p(0) = 0.75$ (both in m) in the beginning. The particle motion is tracked in the time interval of 0–100 s. An equidistant grid is used. The time step size used for the computation is $\Delta t_p = 0.01$ s to ensure that the numerical integration is stable and time stepping errors are small. A comparison of particle trajectory⁸ during the period of 0–100 s for the interpolation scheme shows a good agreement (in Fig. 13a) with that determined analytically using expressions given in Marchioli et al. [27]. Let $w_{fn,i}$ and $w_{fa,i}$ be the numerically computed and analytically determined value of the undisturbed fluid velocity at particle position at i^{th} time step, then the root-mean-square (rms) error in the interpolation of the fluid velocity⁹ $\epsilon_{\text{rms},wf}$ over N number of time steps is given as

$$\epsilon_{\text{rms},wf} = \sqrt{\frac{\sum_{i=1}^N (|w_{fn,i} - w_{fa,i}|)^2}{N}}. \quad (12)$$

⁸ The trajectory of an inertia-free particle is computed by solving Eq. (6) where $\mathbf{u}_p(t) = \mathbf{u}_f(\mathbf{x}_p, t)$.

⁹ Only the w_f component of the fluid velocity is considered for the error estimation because the other components are spatially uniform.

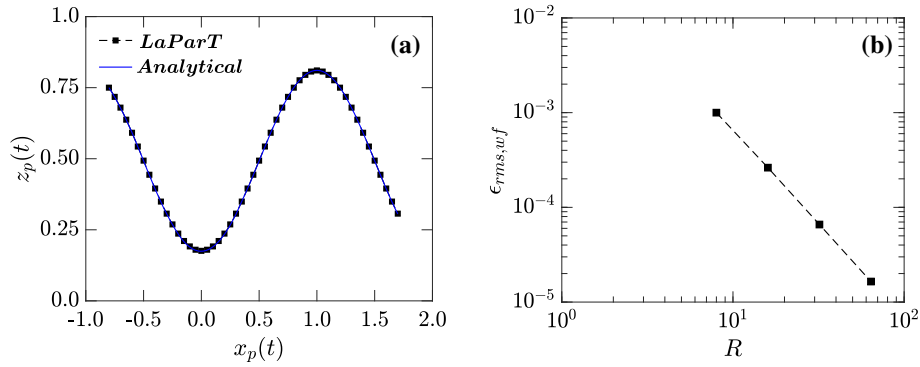


Fig. 13 A single inertia-free particle in a steady, spatially varying sinusoidal flow. **a** Comparison of particle paths computed from the simulation against those using analytical expressions, **b** verification of the order of the fluid velocity interpolation scheme

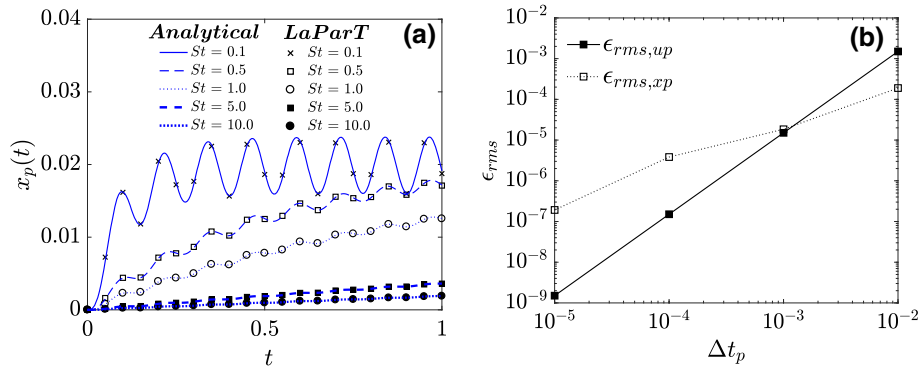


Fig. 14 A single inertial particle in a uniform, transient flow. **a** Comparison of particle trajectory computed from the simulation against those using analytical solution, **b** global error (ϵ_{rms}) in particle velocity (u_p) and displacement (x_p) versus time step size (Δt_p)

Furthermore, we define a grid resolution parameter R to describe the characteristic length scale of the flow λ in comparison to the grid cell thickness Δx as $R = \lambda/\Delta x$, where $\lambda = 2\pi/k_x$. We consider four different grids: coarse $R = 8$, coarse-medium $R = 16$, medium $R = 32$, and fine $R = 64$. As shown in Fig. 13b, the rms error in the fluid velocity interpolation $\epsilon_{rms,wf}$ decreases as the grid resolution improves. We confirm that the trilinear interpolation scheme implemented is second-order accurate (i.e., $\epsilon_{rms,wf}$ decreases at the rate R^{-2}).

1.2. Particle in a spatially uniform but temporally varying flow

This test comprises tracking the motion of an inertial particle in a spatially uniform but temporally varying velocity field in a sinusoidal fashion, as done in Jacobs et al. [45]. The flow velocity field is given by $u_f = \sin(k_f t)$ where $k_f = 16\pi$. The particle is displaced only in the x -direction. We set the particle initial position $x_p(0)$ and velocity $u_p(0)$ to zero. The particle is tracked during the time window between 0 and 1 s. Five different values of the particle Stokes number $St = 0.1, 0.5, 1, 5, \text{ and } 10$ are considered. Here, the particle relaxation time τ_p is normalized using the characteristic flow time scale τ_f to obtain St , where $\tau_f = 1$ s in this problem. The numerically computed instantaneous particle positions $x_p(t)$ match those computed using analytical expressions, as shown in Fig. 14a. (We refer to Jacobs et al. [45] for the analytical expressions of $x_p(t)$.) This match explains that the effect of τ_p on the particle trajectory is captured accurately in the numerical integration. We compute the rms error (ϵ_{rms}) in the calculation of the particle velocity (u_p) and position (x_p) for different time step sizes $\Delta t_p = 10^{-2}, 10^{-3}, 10^{-4}$, and 10^{-5} for a particle with $St = 1$, as shown in Fig. 14b. It is noticed that ϵ_{rms} decreases with a decrease in Δt_p , implying the implemented numerical scheme is convergent. The numerical solutions of particle position and momentum are first- and second-order accurate, respectively.

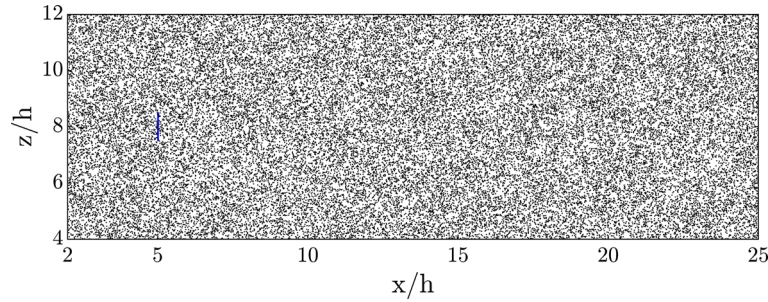


Fig. 15 Distribution of particles with very low inertia (i.e., $St=0.005$) in the unsteady laminar flow over a normal flat plate

1.3 Low inertia particles in the unsteady non-uniform flow

The hydrodynamic response of very low inertia particles to the non-uniform flow is expected to be similar to fluid particles (tracers). Therefore, such tracer-like particles should be distributed uniformly in the unsteady non-uniform flow. The present test verifies that the spatial distribution of tracer-like particles obtained from the numerical solution is consistent with the expected physical behavior. The confirmation would assure that the schemes implemented in LaParT respect the incompressibility constraint. To this end, the unsteady laminar wake behind a normal flat plate is considered a representative non-uniform test flow case. The Reynolds number for the flow based on the uniform inflow velocity (U_c) and plate height (h) is 60, where the unsteady wake behind the plate is characterized with a von Kármán vortex street. Particles with $St=0.005$ (representing significantly low particle inertia) are injected homogeneously near the inlet. A snapshot of the instantaneous distribution of particles in the computation domain taken at $t = 40 h/U_c$ (from the beginning of the particle injection) is shown in Fig. 15. We confirm that the instantaneous spatial distribution of such tracer-like particles is homogeneous throughout the domain, which agrees with the expected physical behavior.

2. Validation of MGLET-LaParT

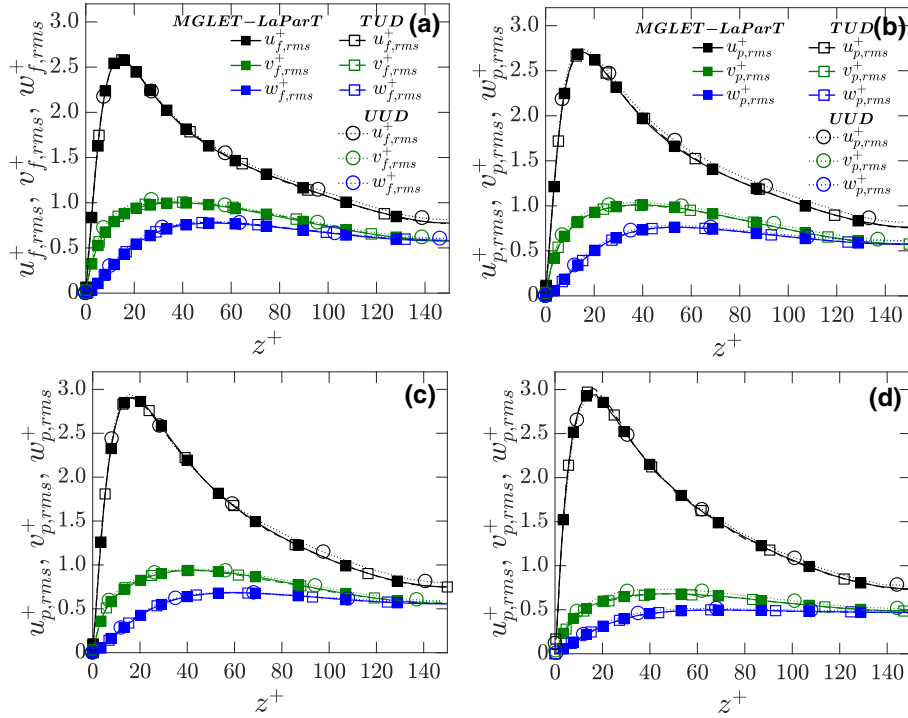
We discuss the validation of MGLET-LaParT using the benchmark particle-laden turbulent flow case of Marchioli et al. [47], where the results of five research groups using different numerical procedures have been documented. We consider the results of TUD and UUD groups for the comparison purpose. The flow configuration and test setup used in our simulation are the same as those of the benchmark validation test and summed up briefly again for the reader's convenience. The validation test investigates the pressure-driven turbulent channel flow of a dilute suspension that comprises many monodispersed, small-sized inertial particles. The friction Reynolds number of the flow, based on the half-channel height h , and friction velocity u_* , is $Re_* = \rho_f u_* h / \mu_f = 150$. Here, the friction velocity is obtained using ρ_f and the mean wall shear stress τ_w as $u_* = \sqrt{\tau_w / \rho_f}$. The channel is positioned such that the Cartesian co-ordinate¹⁰ axes x , y , and z are aligned in the streamwise, spanwise, and wall-normal directions, respectively. Hereafter, simulation parameters given in the wall-units will be denoted using symbols accompanied by a superscript $+$. Such simulation parameters are scaled using the viscous length $l_v = \nu_f / u_*$, time $\tau_v = \nu_f / u_*^2$, and velocity scales u_* . Periodic boundary conditions are imposed in the homogeneous x - and y -directions. The smooth flat walls positioned at $z = 0$ and $z = 2h$ in the inhomogeneous z -direction are treated by imposing the no-slip and non-penetration condition on the carrier fluid. The channel dimensions are $L_x = 12.56h$ ($L_x^+ = 1885$), $L_y = 6.28h$ ($L_y^+ = 942.5$), and $L_z = 2h$ ($L_z^+ = 300$) in the x -, y -, and z - directions, respectively. The constant grid-cell dimensions in the x - and y - directions are $\Delta x^+ = 9.82$ and $\Delta y^+ = 4.91$, respectively. The grid is stretched in the z - direction, where $\Delta z_{\min}^+ = 0.36$, and $\Delta z_{\max}^+ = 4.06$ are, respectively, the minimum (near the wall) and maximum grid-cell dimensions (channel center).

The dispersed phase comprises small-sized, denser-than-fluid, spherical particles. We consider three different cases, each with a unique particle Stokes number St_v (i.e., 1, 5, and 25), where St_v is given as $St_v = \tau_p / \tau_v$. Particle properties in each case are documented in Table 5. We have homogeneously injected a total of 10^5 particles (in each St_v case) into the statistically stationary turbulent carrier flow. Particles are randomly positioned in x - and y -directions with a uniform spacing in the z -direction. The periodic domain is considered for a

¹⁰ The origin of the co-ordinate system is located at (0,0,0).

Table 5 Particle properties

Parameter	Case-1	Case-2	Case-3
St_v	1	5	25
ρ_p/ρ_f	769.23	769.23	769.23
d_p	$1.02 \times 10^{-3}h$	$2.28 \times 10^{-3}h$	$5.10 \times 10^{-3}h$
τ_p (s)	6.67×10^{-3}	3.33×10^{-2}	0.17
d_p^+	0.15	0.34	0.77

**Fig. 16** Root-mean-square of velocity fluctuations. **a** fluid, and particles with **b** $St_v=1$, **c** $St_v=5$, **d** $St_v=25$

particle in the streamwise (x) and spanwise (y) direction. If a particle approaches the smooth flat wall such that the distance between its geometric center and the wall is less than its radius, then this condition is considered as the particle-wall collision event. Such a particle is rebounded back elastically in the domain after the collision. In Fig. 16, a comparison of root-mean-square (rms) fluctuations in the streamwise ($u_{i,rms}^+$), spanwise ($v_{i,rms}^+$), and wall-normal ($w_{i,rms}^+$) velocity components of our simulation with benchmark groups is shown for the fluid ($i = f$; see Fig. 16a) and particle phases ($i = p$; see Fig. 16b–d). With an increase in particle inertia from $St_v=1$ to 25, $u_{p,rms}^+$ values of benchmark results in the near-wall region become larger compared to $u_{f,rms}^+$. On the other hand, $v_{p,rms}^+$ and $w_{p,rms}^+$ values get smaller in magnitude than $v_{f,rms}^+$ and $w_{f,rms}^+$, respectively, with an increase in St_v . This trend is captured in our simulations. Furthermore, a quantitative comparison of profiles for $St_v=1$ (Fig. 16b), $St_v=5$ (Fig. 16c), and $St_v=25$ (Fig. 16d) suggests that our simulation results are in a good agreement with the benchmark data.

References

1. Squires, K.D., Eaton, J.K.: Preferential concentration of particles by turbulence. *Phys. Fluids A* **3**(5), 1169–1178 (1991)
2. Caporaloni, M., Tampieri, F., Trombetti, F., Vittori, O.: Transfer of particles in nonisotropic air turbulence. *J. Atmos. Sci.* **32**(3), 565–568 (1975)
3. Simon, X., Bémer, D., Chazelet, S., Thomas, D., Régner, R.: Consequences of high transitory airflows generated by segmented pulse-jet cleaning of dust collector filter bags. *Powder Technol.* **201**(1), 37–48 (2010)

4. Pan, Y., Si, F., Xu, Z., Romero, C.E., Qiao, Z., Ye, Y.: DEM simulation and fractal analysis of particulate fouling on coal-fired utility boilers' heating surfaces. *Powder Technol.* **231**, 70–76 (2012)
5. Brandon, D.J., Aggarwal, S.: A numerical investigation of particle deposition on a square cylinder placed in a channel flow. *Aerosol Sci. Technol.* **34**(4), 340–352 (2001)
6. Salmanzadeh, M., Rahnama, M., Ahmadi, G.: Particle transport and deposition in a duct flow with a rectangular obstruction. *Part. Sci. Technol.* **25**(5), 401–412 (2007)
7. Afrouzi, H.H., Sedighi, K., Farhadi, M., Moshfegh, A.: Lattice Boltzmann analysis of micro-particles transport in pulsating obstructed channel flow. *Comput. Math. Appl.* **70**(5), 1136–1151 (2015)
8. Jafari, S., Salmanzadeh, M., Rahnama, M., Ahmadi, G.: Investigation of particle dispersion and deposition in a channel with a square cylinder obstruction using the lattice Boltzmann method. *J. Aerosol Sci.* **41**(2), 198–206 (2010)
9. Bagheri, M., Sabzpooshani, M.: On the importance of the history force in dispersion of particles in von Kármán vortex street. *Adv. Powder Technol.* **31**(9), 3897–3909 (2020)
10. Yao, J., Zhao, Y., Hu, G., Fan, J., Cen, K.: Numerical simulation of particle dispersion in the wake of a circular cylinder. *Aerosol Sci. Technol.* **43**(2), 174–187 (2009)
11. Haugen, N.E.L., Kragset, S.: Particle impaction on a cylinder in a crossflow as function of Stokes and Reynolds numbers. *J. Fluid Mech.* **661**, 239 (2010)
12. Zhou, H., Mo, G., Cen, K.: Numerical investigation of dispersed gas-solid two-phase flow around a circular cylinder using lattice Boltzmann method. *Comput. Fluids* **52**, 130–138 (2011)
13. Shi, Z., Jiang, F., Strandenes, H., Zhao, L., Andersson, H.I.: Bow shock clustering in particle-laden wetted cylinder flow. *Int. J. Multiph. Flow* **130**, 103332 (2020)
14. Shi, Z., Jiang, F., Zhao, L., Andersson, H.I.: Clusters and coherent voids in particle-laden wake flow. *Int. J. Multiph. Flow* **141**, 103678 (2021)
15. Ghafouri, S., Alizadeh, M., Seyyedi, S., Afrouzi, H.H., Ganji, D.: Deposition and dispersion of aerosols over triangular cylinders in a two-dimensional channel; effect of cylinder location and arrangement. *J. Mol. Liq.* **206**, 228–238 (2015)
16. Wang, H., Agrusta, R., van Hunen, J.: Advantages of a conservative velocity interpolation (CVI) scheme for particle-in-cell methods with application in geodynamic modeling. *Geochem. Geophys. Geosyst.* **16**(6), 2015–2023 (2015)
17. Chein, R., Chung, J.: Particle dynamics in a gas-particle flow over normal and inclined plates. *Chem. Eng. Sci.* **43**(7), 1621–1636 (1988)
18. Gomes, M.S., Vincent, J.H.: The effect of inertia on the dispersion of particles in the flow around a two-dimensional flat plate. *Chem. Eng. Sci.* **57**(8), 1319–1329 (2002)
19. Cheng, M., Tan, S., Hung, K.: Linear shear flow over a square cylinder at low Reynolds number. *Phys. Fluids* **17**(7), 078103 (2005)
20. Lankadasu, A., Vengadesan, S.: Onset of vortex shedding in planar shear flow past a square cylinder. *Int. J. Heat Fluid Flow* **29**(4), 1054–1059 (2008)
21. Peller, N., Duc, A.L., Tremblay, F., Manhart, M.: High-order stable interpolations for immersed boundary methods. *Int. J. Numer. Meth. Fluids* **52**(11), 1175–1193 (2006)
22. Manhart, M.: A zonal grid algorithm for DNS of turbulent boundary layers. *Comput. Fluids* **33**(3), 435–461 (2004)
23. Stone, H.L.: Iterative solution of implicit approximations of multidimensional partial differential equations. *SIAM J. Numer. Anal.* **5**(3), 530–558 (1968)
24. Maxey, M.R., Riley, J.J.: Equation of motion for a small rigid sphere in a nonuniform flow. *Phys. Fluids* **26**(4), 883–889 (1983)
25. Armenio, V., Fiorotto, V.: The importance of the forces acting on particles in turbulent flows. *Phys. Fluids* **13**(8), 2437–2440 (2001)
26. Mollicone, J.-P., Sharifi, M., Battista, F., Gualtieri, P., Casciola, C.M.: Particles in turbulent separated flow over a bump: Effect of the Stokes number and lift force. *Phys. Fluids* **31**(10), 103305 (2019)
27. Marchioli, C., Armenio, V., Soldati, A.: Simple and accurate scheme for fluid velocity interpolation for Eulerian–Lagrangian computation of dispersed flows in 3D curvilinear grids. *Comput. Fluids* **36**(7), 1187–1198 (2007)
28. Arcen, B., Tanière, A., Oesterlé, B.: On the influence of near-wall forces in particle-laden channel flows. *Int. J. Multiph. Flow* **32**(12), 1326–1339 (2006)
29. Schiller, L., Naumann, A.: Fundamental calculations in gravitational processing. *Z. Ver. Dtsch. Ing.* **77**, 318–320 (1933)
30. Minier, J.-P., Peirano, E.: The pdf approach to turbulent polydispersed two-phase flows. *Phys. Rep.* **352**(1–3), 1–214 (2001)
31. Subramaniam, S.: Lagrangian-Eulerian methods for multiphase flows. *Prog. Energy Combust. Sci.* **39**(2–3), 215–245 (2013)
32. Minier, J.-P.: Statistical descriptions of polydisperse turbulent two-phase flows. *Phys. Rep.* **665**, 1–122 (2016)
33. Singh, A., Narasimhamurthy, V.D.: DNS of wake from perforated plates: aspect ratio effects. *Prog. Comput. Fluid Dyn.* **21**(6), 355–368 (2021)
34. Narasimhamurthy, V.D., Andersson, H.I.: Numerical simulation of the turbulent wake behind a normal flat plate. *Int. J. Heat Fluid Flow* **30**(6), 1037–1043 (2009)
35. Narasimhamurthy, V.D., Andersson, H.I., Pettersen, B.: Steady viscous flow past a tapered cylinder. *Acta Mech.* **206**(1), 53–57 (2009)
36. Saha, A.K.: Far-wake characteristics of two-dimensional flow past a normal flat plate. *Phys. Fluids* **19**(12), 128110 (2007)
37. Monchaux, R., Bourgoin, M., Cartellier, A.: Analyzing preferential concentration and clustering of inertial particles in turbulence. *Int. J. Multiph. Flow* **40**, 1–18 (2012)
38. Nilsen, C., Andersson, H.I., Zhao, L.: A Voronoi analysis of preferential concentration in a vertical channel flow. *Phys. Fluids* **25**(11), 115108 (2013)
39. Fong, K.O., Amili, O., Coletti, F.: Velocity and spatial distribution of inertial particles in a turbulent channel flow. *J. Fluid Mech.* **872**, 367–406 (2019)
40. Bouris, D., Papadakis, G., Bergeles, G.: Numerical evaluation of alternate tube configurations for particle deposition rate reduction in heat exchanger tube bundles. *Int. J. Heat Fluid Flow* **22**(5), 525–536 (2001)

41. Tong, Z.-X., Li, M.-J., He, Y.-L., Tan, H.-Z.: Simulation of real time particle deposition and removal processes on tubes by coupled numerical method. *Appl. Energy* **185**, 2181–2193 (2017)
42. Wagner, R.: Multi-linear interpolation. Beach Cities Robotics (2008). <http://rjwagner49.com/Mathematics/Interpolation.pdf>. Accessed 18 October 2018
43. Meyer, D., Jenny, P.: Conservative velocity interpolation for PDF methods. *Proc. Appl. Math. Mech.* **4**(1), 466–467 (2004)
44. Rouson, D.W.: A direct numerical simulation of a particle-laden turbulent channel flow (1998)
45. Jacobs, G.B., Kopriva, D.A., Mashayek, F.: Towards efficient tracking of inertial particles with high-order multidomain methods. *J. Comput. Appl. Math.* **206**(1), 392–408 (2007)
46. Kontomaris, K., Hanratty, T., McLaughlin, J.: An algorithm for tracking fluid particles in a spectral simulation of turbulent channel flow. *J. Comput. Phys.* **103**(2), 231–242 (1992)
47. Marchioli, C., Soldati, A., Kuerten, J., Arcen, B., Taniere, A., Goldensoph, G., Squires, K., Cargnelutti, M., Portela, L.: Statistics of particle dispersion in direct numerical simulations of wall-bounded turbulence: results of an international collaborative benchmark test. *Int. J. Multiph. Flow* **34**(9), 879–893 (2008)
48. Marchioli, C., Picciotto, M., Soldati, A.: Influence of gravity and lift on particle velocity statistics and transfer rates in turbulent vertical channel flow. *Int. J. Multiph. Flow* **33**(3), 227–251 (2007)

Publisher's Note Springer Nature remains neutral with regard to jurisdictional claims in published maps and institutional affiliations.

Springer Nature or its licensor holds exclusive rights to this article under a publishing agreement with the author(s) or other rightsholder(s); author self-archiving of the accepted manuscript version of this article is solely governed by the terms of such publishing agreement and applicable law.